Nucl. Instr. & Meth. A, revised Nov 2007

High resolution synchrotron-based radiography and tomography using hard X-rays at the BAM*line* (BESSY II)

A. Rack and S. Zabler

Hahn-Meitner-Institut Berlin, Department Materials – SF3,

*Glienicker Str. 100, D-14109 Berlin, Germany**

B. R. Müller, H. Riesemeier, G. Weidemann, A. Lange, J. Goebbels, M. Hentschel, and W. Görner

Bundesanstalt für Materialforschung und -prüfung,

Divisions Radiology – I.4 and Process Analysis – VIII.3,

Unter den Eichen 80, D-12205 Berlin, Germany

(Dated: November 7, 2007)

Abstract

The use of high brilliance and partial coherent synchrotron light for radiography and computed tomography (CT) allows to image micro-structured, multi-component specimens with different contrast modes and resolutions up to submicrometer range. This is of high interest for materials research, life science and non-destructive evaluation applications. An imaging setup for microtomography and -radiography installed at BESSY II (a third generation synchrotron light source located in Berlin, Germany) as part of its first hard X-ray beamline (BAM*line*) can now be used for absorption, refraction as well as phase contrast – dedicated to inhouse research and applications by external users. Monochromatic synchrotron light between 6 and 80 keV is attained via a fully automated double multilayer monochromator. For imaging applications the synchrotron beam transmitted by the sample is converted with a scintillator into visible light, by use of microscope optics this luminescence image is then projected onto, e.g., a CCD chip. Several scintillating materials are used in order to optimise the performance of the detector system. Different optical systems are available for imaging ranging from a larger field of view and moderate resolutions (macroscope – up to 14 mm x 14 mm field of view) to high resolution (microscope – down to 0.35 μm pixel size), offering magnifications from 1.8x to 40x. Additionally asymmetric cut Bragg crystals in front of the scintillator can be used for a further magnification in one dimension by a factor of 20. Slow and fast cameras are available, with up to 16 bit dynamic range. We show the suitability of the setup for numerous applications from materials research and life science.

Keywords: microtomography, non-destructive evaluation, synchrotron instrumentation, coherent imaging, X-ray refraction, phase contrast, holotomography, Synchrotron-CT, scintillator, Bragg magnification

*Corresponding author's current address: A. Rack, Forschungszentrum Karlsruhe, Institute for Synchrotron Radiation, Hermann-von-Helmholtz-Platz 1, 76344 Eggenstein-Leopoldshafen, Germany, e-mail: `arack@snafu.de`

I. INTRODUCTION

Since the discovery of X-rays by W. C. Röntgen [1] non-destructive imaging of objects has proven to be a powerful tool in diverse fields such as medicine, materials research, archaeology, quality control or homeland security. While for many tasks the two dimensional radiographic projection imaging is suitable, specifically with short acquisition times, there is much need for obtaining, in a non-destructive manner, information about the three-dimensional structure of objects. A. M. Cormack published his approach in the 1960's to derive the mass distribution inside an object from its radiographic projection images taken from different projection angles [2]. Based on this idea G. N. Hounsfield introduced in the 1970's the first scanner for non-invasive three-dimensional imaging – so called computed tomography (CT) [3]. Following the huge success of CT in medicine [4] this method was soon utilized in materials research and non-destructive testing as well [5, 6]. With microfocus X-ray tubes spatial resolutions up to the micrometer scale can be reached – μCT [7]. Compared to laboratory X-ray sources, synchrotron radiation offers a significant improvement with its nearly parallel beam propagation, a flux which is several orders of magnitudes higher and the possibility to work with a monochromatic beam. These advantages lead to higher reconstruction qualities, fewer artifacts, shorter acquisition times and improved contrast [7–9]. The fundamentals of synchrotron-based microtomography and -radiography are known since the 1990's [8, 10] with available resolutions up to submicrometer [11].

This article describes the imaging setup of the BAM*line* at the German storage ring BESSY (Berliner Elektronenspeicherring – Gesellschaft für Synchrotronstrahlung m.b.H.). BESSY is a third generation synchrotron light source operating since 1998 with a ring energy of 1.7 GeV [12]. The BAM*line* is BESSY's first hard X-ray beamline using a superconducting 7T wavelength shifter as insertion device, operated by the Bundesanstalt für Materialforschung und -prüfung (Federal Institute for Materials Research and Testing – BAM), Germany [13, 14]. The beamline is dedicated to host several experimental methods, including an imaging facility since 2001 [15]. Synchrotron microtomography was started at the BAM*line* by the BAM as it extends perfectly their capabilities based on the laboratory CT equipment [9]. The setup is operated and developed further jointly by the BAM and the Hahn-Meitner-Institut Berlin (Germany) since 2003. The demand for microtomography experiments at synchrotron light sources is permanently increasing since the end of the

1990's, making it more and more difficult to get beamtime on already established imaging facilities. With the installation of the imaging setup at the BAM*line* we can offer, similiar to other synchrotron light sources like ESRF [16], SLS [17], HASYlab [18], SPRING8 [19], APS [20, 21] high resolution synchrotron microtomography to scientific and commercial users for performing excellent science and relevant technological development.

Due to the partial spatial coherence of synchrotron radiation more sophisticated contrast modes can be used. For some applications this may be better than imaging the linear attenuation coefficient in standard μCT. Examples are phase contrast and holotomography (imaging the local electron density [22–25]) which are of interest in materials research [16, 26]. Furthermore, the high synchrotron flux enables us to perform refraction enhanced tomography (sensitive to inner surfaces and interfaces [27]) and to use asymmetric cut Bragg crystals for further magnification in one dimension, extending the resolution up to the nanoscale. The implementation of these methods is described in this article as part of the instrumentation, applications are introduced within dedicated sections.

II. EXPERIMENTAL SETUPS FOR IMAGING

A. BAM*line*

1. *Beamline layout and instrumentation*

The optical section of the BAM*line* is sketched in fig. 1. The synchrotron light coming from the superconducting 7T wavelength shifter insertion device can be monochromatized with a double multilayer monochromator (DMM) and/or a double crystal monochromator (DCM), a vertical focusing option is available for the DMM and a horizontal focusing option for the DCM. Slits are positioned upstream (aperture) and downstream of the monochromators as well as in the experimental hutch. Several polished metal foils placed in front of the DMM are used to absorb low energy X-rays which otherwise would be transmitted by the DMM by total reflection and consequently deteriorate the DMM's monochromaticity. The filters also lower the heat load on the first multilayer mirror. For monochromaticity reasons as well the layer-structure of the DMM has been optimized to suppress higher harmonic wavelengths (the multilayer coating consists of 150 double layers W/Si leading to an energy bandwidth of 1.7% in the range between 5 and 50 keV – experimentally verified at 20 keV

with an DCM energy scan downstream of the DMM). The beamline can also be operated in white beam mode [13, 14].

The flux measured downstream of the DMM is plotted for different photon energies in fig. 2. Due to the limited amount of photons available only the DMM is used for microtomography at the BAM*line* (see section III).

The source-to-sample distance at the BAM*line* is 35 m (see fig. 1). Even when assuming a relatively large source size of 200 μm (see next paragraph) and a typical sample to detector distance of 10 mm the image blurring resulting from the finite source size is smaller than 0.1 μm and hence has no influence on high resolution imaging (e.g. by penumbral blurring).

2. Requirements for coherent imaging techniques

In addition to the requirements that are mandatory for recording high resolution X-ray attenuation maps, coherent imaging techniques such as phase contrast and holotomography introduce further demands on the beamline. Among these monochromaticity is the most fundamental, but also the less stringent. Although the energy spread of the double multilayer monochromator at BAM*line* is approx. 1.7%, imaging relatively thick (up to several millimeters) samples under quasi-coherent conditions is feasible, despite of the fact that the longitudinal coherence length $l_L = \lambda^2/\triangle\lambda$ here is in the order of 0.01 μm. An intuitive explanation for the discrepancy between sample thickness and coherence length is that only the local phase modulations inside the sample, not the integral phase shift produce the interference fringes forming phase contrast images [28].

Concerning the image resolution there are smaller and larger length scale limitations for coherent imaging. The larger limit is determined by the X-ray wavelength and the thickness t of the sample which causes an image blurring due to Fresnel-propagation inside the sample and is given by $\sqrt{t\lambda} \approx 0.3$ μm (for $t = 1$ mm and $\lambda = 1$ $\mathring{A}$) [28]. An estimate for the minimum resolution can be derived from the visibility of the fringes which is approx. 10 μm (as observed during feasibility studies). The optical parameters of the BAM*line* microscope have been selected to cover the entire range between these two limits (cf. table I).

The transverse coherence length l_T is determined by the angular divergence of the X-ray source projected from the object to the detector. For a given angular divergence α and

wavelength λ the coherence length is given by [29]:

$$l_T = \frac{\lambda}{2\alpha} \tag{1}$$

thus defining an interference condition for two distinct waves of the incident beam. In most cases one can assume a Gaussian intensity distribution of the source and replace the angular divergence by the lateral extension of the source s $= \alpha z_1$, with z_1 the distance from the source to the object. The blurring of the image due to the finite source size is then simply the projection of the source and calculated by sz_2/z_1, with z_2 the distance from the object to the image plane. Due to a small magnification we have to replace z_2 by $D = z_1 z_2/(z_1 + z_2)$, which we will refer to as the propagation distance. At the BAM*line* we have $z_1 \approx 35$ m and a translation of the camera with respect to the sample of $z_2 = 0.005 \ldots 1.125$ m, therefore the maximum propagation distance is $D = 1.09$ m.

For measuring the transverse coherence length and thus the effective angular source size (keeping in mind that we have components such as the monochromator between the sample and our source) we used Talbot imaging [30–32] of two dimensional phase gratings. We used three gratings with rectangular profiles (2.9 μm high) etched into a flat silicon substrate [28]. The periodicity of the gratings were 4 μm, 6 μm and 8 μm respectively. First, second and third harmonics of the patterns were measured by Fourier-transforming radiographs of the gratings taken at different propagation distances which correspond to multiples of half the Talbot distance. In the ideal case of a perfectly coherent point source a diffraction order n of a grating of periodicity p would be reproduced identically at multiples of the Talbot distance $D_T = 2p^2/(n\lambda)$, here we used an X-ray energy of 17.1 keV (corresponds to $\lambda = 0.725$ Å). One can calculate that an image taken at half the Talbot distance is shifted by half the period with respect to the initial image and therefore produces the same magnitude of the different diffraction orders. Supposing a Gaussian envelope of the source in Fourier space

$$\tilde{\mathrm{Q}}(Dn/p) = exp\left(-2\left(\pi\sigma_\alpha D\frac{n}{p}\right)^2\right)$$

with σ_α related to the angular source size via $\alpha = 2.35\sigma_\alpha$. The angular source size is then calculated from the amplitude ratio of the diffraction order n calculated from two radiographs I_0 and I_1 taken at distances D_0 and D_1, separated by half the corresponding

Talbot distance:

$$\alpha = \frac{2.35 \cdot p}{n\pi\sqrt{2(D_1^2 - D_0^2)}}\sqrt{ln\left|\frac{\tilde{\mathrm{I}}_0^n}{\tilde{\mathrm{I}}_1^n}\right|} \quad \text{with} \quad D_1 = D_0 + \frac{D_T}{2}$$

As a result we obtain an angular divergence of 1.16 ± 0.21 μrad in the vertical plane and 4.69 ± 0.17 μrad in the horizontal plane. The corresponding effective vertical source size is 40.6 ± 7.2 μm and the horizontal size 164.0 ± 5.8 μm (FWHM). The larger horizontal spread of the source is a consequence of the electron trajectory in the insertion device.

From these observations we can determine the transverse coherence length l_T according to equation 1 obtaining approx. 8 μm in the horizontal and 31 μm in the vertical direction. These values must be compared to the fringe spacing in the propagated images given by $\sqrt{\lambda D}$. For the given wavelength $\lambda = 0.725$ Å (17.1 keV) and the maximum propagation distance D = 1.09 m we obtain a spacing of approx. 9 μm. Therefore further extending the range of the sample-to-detector distances would not allow us to image the interference fringes more efficiently, at least not in the horizontal direction. Fig. 3 shows the effective three-dimensional shape of the X-ray source intensity distribution based on these Talbot measurements.

B. Manipulators

The BAM*line* is designed as a multi purpose beamline [13] with the possibility of mounting different setups for: X-ray fluorescence analysis [14], topography [33], absporption spectroscopy [34, 35], reflectometry [35], detector calibration and characterization [36], dosimetry [37], imaging and any in-house constructed user experiment. In order to minimize the setup time prior to the experiment for the micro-imaging station we constructed a table which can be fast installed and aligned (parallel to the beam path) – see fig. 4. This table can be moved in and out of the experimental hutch for a fast and complete exchange with other setups and comprises the motorized sample stage as well as a one meter linear stage with the detector system. The whole setup can be lifted or lowered and pivoted to adjust pitch and yaw in order to align the camera translation parallel to the beam.

In order to align our sample and to perform micro- and holotomography x-, y-, z-stages as well as roll and yaw positioning devices are required. A cradle is used in order to align the axis of rotation perpendicular to the beam propagation direction and along the CCD chips

orientation and the raw adjustment of the sample height is done with a z-stage (HUBER Diffraktionstechnik GmbH & Co. KG). For the tomography itself high precision linear (brightfield / flatfield images) and rotation stages (different projection angles) are used (Micos GmbH Germany). The one meter linear stage is an airbeared table with 1100 mm travel range (Johann Fischer Aschaffenburg GmbH): pitch and raw approx. 10 μrad with a maximum load of 60 kg. Two detectors (macroscope and microscope – see next section) can be mounted on the stage which is used to vary the distance between detector and sample (phase contrast and holotomography – see paragraph IV).

For the refraction enhanced imaging (see paragraph V) a second experimental station is permanently installed downstream of the CT position – see fig. 5. To handle the alignment of the corresponding monochromator and analyzer crystal as well as the camera system (macroscope – see next section) a 6-circle goniometer (HUBER Diffraktionstechnik GmbH & Co. KG) is used. The main Theta-2Theta goniometer carries the monochromator crystal (Theta circle) and the secondary goniometer. The secondary Theta-2Theta goniometer carries the analyzer crystal (Theta circle) and the detector system (2Theta arm), respectively (cf. fig. 5). This allows the rotation of the analyzer crystal around the monochromator crystal and the rotation of the camera system around the analyzer crystal according to the chosen photon energy. Each crystal is fixed to a separate motorized goniometer head, which allows a fine adjustment (x, y, z, roll and yaw) of the crystal surface with respect to the axis of rotation of the goniometer. All axes of rotation are oriented horizontally and perpendicular to the beam axis. The entire goniometer is mounted onto a lift for changing a beam position at different photon energies and beam offsets. For refraction enhanced imaging measurements the sample manipulator system is mechanically separated from the 6-circle goniometer. Its components are of identical type, quality and functionality as used for the CT measurements.

C. Detectors

Besides a high precision sample manipulator the important device for microtomography is a digital detector-microscope suitable to obtain highly resolved radiographic images. The design of our detector follows the concepts of U. Bonse and F. Busch [8]: a luminescence screen is imaged via microscope optics onto a CCD chip, see fig. 6. The luminescence screen

is a scintillator in powder form or as single crystal, commonly fixed on a substrate. The optical path is folded by using a mirror in order to keep the CCD camera out of the intense synchrotron radiation beam. The effective magnification of this optical system can be chosen via the ratio of the applied light optics focal lengths and optionally by using an eye-piece between the tube lens and the CCD. The maximal lateral resolution is determined by the microscope optics, the luminescence screen, the CCD chip, and the sampling theorem and can be extended up to the submicrometer range [11]. Additionally we installed glas filters and a diaphragm in the optical path. The diaphragm is a thin opaque light stop with an adjustable aperture (the centre of the aperture is aligned with the optical axis of the macroscope). A colored glas filter can be used to suppress luminescence light emitted by a substrate. It is also used to filter scintillation light from the screen beyond the chromatic correction of the optics. Instead of glas filters optical band passes can also be applied. Since the full well capacity per pixel of a CCD is limited but one wants to exploit the dynamic range of the camera's chip we have to optimize the ratio of detected luminescence photons (CCD) vs. converted X-ray photons (luminescence screen). Otherwise, as a single high-energy X-ray can be converted into few hundreds of visible low-energy photons, one risks an increased signal-to-noise ratio. The optimization can be achieved by adapting the diaphragm (which can also be useful to trim the numerical aperture (NA) of the optics [11]) or alternatively by inserting neutral density filters into the optical path. In the ideal case, each absorbed X-ray in the screen should lead to one digital count in the CCD chip – resulting in a high dynamic X-ray imaging detector. Descriptions of the cameras and optical systems used (macroscope and microscope) are given in the following sections.

1. Scintillators

As described in section II A the superconducting 7T wavelength shifter in combination with a double multilayer monochromator delivers a moderate X-ray flux compared to other imaging beamlines at third generation light sources [17, 18, 21, 38, 39]. This is a major drawback, specially for high resolution tomography or fast radiography as these experiments require a high flux in order to keep the exposure times below a reasonable amount. Scintillating materials with a high stopping power are needed in order to use as many photons as possible in combination with high resolution imaging. The high quantum efficiency over a

broad spectral bandwidth of the Princeton Instruments cameras (see section II C 4) allows us a choice between a wide range of scintillating screens as their maximal emission wavelength varies between 400 nm and 700 nm (cf. table II). Polished single crystal wafers with parallel surfaces are the first choice for luminescence screens in order to minimize blurring of the images by internal scattering of visible light. The remaining limiting factors for the resolution are the depth of focus of the microscope optics used and scattering of the X-rays inside the scintillator. These problems were investigated intensively via numerical simulations, providing crystal thicknesses optimized for the respective resolution in combination with a maximized stopping power [11, 17].

For resolutions ranging from 10 to 20 μm Gadox (Gd_2O_2S:Tb, Proxitronic GmbH) powder screens on glas substrate were used. For higher resolutions cerium doped YAG ($Y_3Al_5O_{12}$:Ce, Saint-Gobain Crystals) single crystals grown on top of undoped YAG substrates were applied [15, 40]. Both materials are well-known and customized screens are commercially available. Gadox has a high stopping power and high light yield (conversion rate from X-ray energy into visible light, assumed to be constant for the X-ray energy range used). Nearly perfect homogeneous screens are available but suffer from light scattering on the powder particles boundaries. As a result, the achievable resolution is limited to approx. the thickness of the screen [41]. YAG:Ce single crystals yield significantly sharper images but the material has a low stopping power, specifically at X-ray energies below 17 keV (see fig. 7).

An optimized scintillator-concept based on known materials [42] was established where the screen used is selected by standard criterions in order to achieve an optimized performance. Depending on the X-ray energy, the scintillating crystal has to be chosen with the maximal stopping power for minimal exposure times – cf. fig. 7. The resolution to be reached defines the maximal thickness of the active layer of scintillation, the maximal polished area available determines the scintillator for moderate resolutions where larger objects are imaged. Finally the imaging speed has to be considered, e.g. minimal afterglow times are required for fast radiography. Four different materials fit these requirements for reasons given below [43].

- CWO ($CdWO_4$) performs with high light yield and excellent stopping power which is up to one order of magnitude higher compared to YAG:Ce (cf. fig. 7), non-treated single crystals are available in nearly any size. Polished crystals can be made with

area diameters of several centimeters and a minimal thickness down to 40 μm. Being among the most oldest scintillating materials known [44], CWO was suggested for synchrotron-based microtomography already in the 1980s [45] and has proven since that to be useful for high resolutions [20, 46] besides high energy applications. The main drawback is the material's high fissionability which limits the achievable minimal thickness via polishing methods. CWO grown by liquid phase epitaxy should overcome this problem but is so far not commercially available. The highest resolution achievable with polished CWOs is approx. 2 μm with X-ray energies below 20 keV where only a thin active layer emits light due to the small penetration depth of the X-ray photons [46]. We obtained our raw crystals from the Ukrainian STRCI – STC "Institute for Single Crystals" [47], polished by the FEE GmbH (Germany).

- BGO ($Bi_4Ge_3O_{12}$) is suited for high energy application fields due to its prominant stopping power at various energy ranges (cf. fig. 7). BGO has been used for positron emission tomography (PET) before the introduction of LSO:Ce [48] but was also quite early suggested for synchrotron microtomography [8]. Non-treated single crystals can be thinned down via polishing processes to a minimal thickness of 25 μm with area diameters of up to several centimeters. No liquid phase epitaxy grown thin crystals in thin layers are available. Its major drawback is the low light yield and therefore BGO is used mainly with large numerical aperture optics.

- LuAG:Eu ($Lu_3Al_5O_{12}$ europium doped) – in order to combine high stopping power with thin active layers (down to 5 μm for submicrometer resolution [11]) the CEA-LETI (France) together with the Special Detectors Group of the European synchrotron ESRF developed further the scintillator-concept based on garnets. In order to increase the stopping power LuAG thin films were grown by liquid phase epitaxy (LPE) on pre-defined, undoped YAG substrates, activated with europium [49]. The substitution of yttrium by lutetium in the garnet structure leads to a significant higher stopping power comparable to those of CWO (cf. fig. 7). Liquid phase epitaxy allows to create high quality thin scintillating LuAG:Eu single crystals with thicknesses ranging from one to several hundreds of micrometer. The area is limited by the dimensions of the crucible used for the LPE process, in our case approx. 25 mm (CEA-LETI, on substrates by the FEE GmbH Germany). Thicknesses of 20 μm and 4 μm are now available at

BAM*line* for resolutions of 2 μm, 1.5 μm and submicrometer. The next step in the garnet evolution for scintillating purposes is GGG:Eu with a higher light yield and a non-scintillating substrate [50], but so far these screens are not commercially available.

- LSO:Ce (Lu_2SiO_5 cerium doped) is the crystal of choice for PET due to its high stopping power, high light yield and an outstanding fast response time [51, 52]. By the late nineties LSO:Ce was already suggested for synchrotron microtomography [11] and is currently used for that as part of a Hamamatsu camera design at SPRing8 [38]. LSO:Ce was successfully tested at BAM*line* with a 25 μm thick crystal glued on glass (kindly provided by the Special Detectors Group of the ESRF). LSO:Ce is patent protected and exclusively available via Siemens Medical Solutions USA, Inc. (Molecular Imaging). It can be replaced by LYSO:Ce [53].

For imaging features at submicrometer resolution, LuAG:Eu single crystals grown by liquid phase epitaxy are used. For moderate resolutions several alternatives exist depending on the stopping power for optimal duty cycles (the fraction of exposure time and read-out time on the whole time amount required for acquiring a low noise image). For fast imaging LSO:Ce or LYSO:Ce are most suitable.

2. Macroscope

In order to investigate larger objects a dedicated optical setup for moderate resolutions (macroscope) has been designed by the BAM CT group with a corresponding field of view of up to 14 mm $\times$ 14 mm (see figures 4 and 6) [9, 15]. The system is housing a commercial photo objective Nikon *Nikkor 180/2.8 ED* (f = 180 mm) as tube lens due to its high quality imaging and high light throughput. For the microscope objectives Rodenstock optics [54] are used due to their high field of view in combination with large numerical apertures in the range of 0.5 (low-magnifying microscope objectives work with NA's smaller 0.09 – a bottleneck for the amount of detectable visible photons). The macroscope is modular so that any F-mount camera, e.g. slow scan CCDs for tomography and CMOS cameras for fast radiography, can be used with any objective attached. Three Rodenstock optics are mounted on individual holders to allow a fast exchange: a) *TV-Heligon* (f = 21 mm, 8.6x with Nikon objective, NA=0.5), b) *TV-Heliflex* (f = 50 mm, 3.6x with Nikon objective, NA=0.45) and c)

XR-Heliflex (f = 100 mm, 1.8x with Nikon objective, NA=0.33). All components facing the beam are made from 10 mm thick brass in order to protect the optics and electronics from synchrotron radiation: specially scattered high energy X-rays directly hitting the CCD chip produce bright spots in the image which cause artifacts in the reconstructed tomographic volumes. Brass was chosen for the shielding as it is easy to machine, mechanical more stable compared to e.g. lead, highly efficient and available for an affordable price. The actual resolution and field of view of the complete detector depends on the applied CCD chips' intrinsic pixel size and dimensions. For example by combining the Princeton Instruments camera *VersArray: 2048B* with the Nikon *Nikkor 180/2.8 ED* and Rodenstock *XR-Heliflex* we obtain an effective pixel size of approx. 7 μm with a field of view of 14 mm $\times$ 14 mm and a resolution of approx. 20 μm (10% of the modulation transfer function (MTF) [55]). By using the *TV-Heligon* the resolution increases to approx. 4 μm with a 3 mm $\times$ 3 mm field of view (see table III). The chromatical correction of the Rodenstock objectives is acceptable between 490 nm and 560 nm. Therefore this optical setup is used in combination with BGO and CWO scintillating single crystals and a 495 nm high-pass glas filter (Thorlabs *FGL495*) [43, 54] or a Gadox powder screen (see section II C 1). A diaphragm inside the optical path is used in order to adjust the numerical aperture of the optics for the aimed resolution [11] as well as to optimize the ratio of absorbed X-rays (luminescence screen) vs. detected visible light photons (CCD). This unique macroscope design allows us to investigate objects with diameters of up to 14 mm with moderate resolutions and optimal duty cycles as we can avoid small NA bottlenecks. The system has already been proven as a powerful tool for synchrotron microtomography in materials research [43, 56–58].

3. Microscope

For high resolution imaging a commercial microscope system is used (Optique Peter – Optical and Mechanical Engineering, France). The original design has been developed in close cooperation between the ID22 group of the European synchrotron ESRF and Optique Peter [39]. This microscope has already been proven to be excellently suited for (synchrotron) microtomography and has been delivered (in modified versions) to other groups as well: Swiss Light Source (SLS) [17], RWTH Aachen / TU Dresden [59], and Angströmquelle Karlsruhe (ANKA) [60].

The microscope section is constructed comparable to a common light microscope with a revolver objective holder for up to three different objectives, motorized in order to switch online between different resolutions. It combines 2x, 4x, 10x and 20x objectives (Olympus) with a 2x eye-piece in order to obtain resolution from several micrometer up to the submicrometer range (cf. table I). A motorized focus and scintillator holders are used for remote and swift exchange of the energy range or the resolution. The CCD cameras are directly mounted on the microscope's body, which is attached to a linear table (Johann Fischer Aschaffenburg) allowing precise positioning at any distance between 5 mm and 1100 mm from the sample. The setup is shown in fig. 4. Glas filters are used in the optical path as well as neutral density filters to optimize the ratio of absorbed X-ray photons (scintillator) vs. detected luminescence photons (CCD).

Colored glas filters are used here to suppress emitted light coming from the substrate of the luminescence screens only. Usually our scintillating single crystals (polished or grown by liquid phase epitaxy) are on top of undoped YAG substrates (see also paragraph II C 1). This material has a strong emission around 400 nm [42] which has to be suppressed in any case with a high-pass filter (Thorlabs *FGL495*), otherwise a significant blurring of the images is the result. A second weaker emission is located around 550 nm [42, 61] which can have an influence when combining for high resolutions thin active layers with high energies. In this case only a few percent of the X-rays are converted in the active layer, the remaining in the substrate which can also lead to a blurring. A stronger high-pass, e.g. Thorlabs *FGL600*, is recommended in this case [43].

For the characterization of the resolving power of our system, we used a commercial X-ray test pattern (Xradia X500-200-30) consisting of line pairs and a Siemens star (a pattern consisting of high absorbing / black lines on a white background – the lines radiate from a center and their thickness increases with increasing distance from the centre). The left picture in fig. 8 shows the complete test pattern, projected onto the CCD using a 8x magnification and a resulting effective pixel size of 1.7 μm. The vertical line pairs have been imaged using a 40x magnification and an effective pixel size of 0.35 μm (4 μm thick LuAG:Eu scintillating single crystal, 15 keV X-ray energy) – see fig. 8 right picture: features with a submicrometer size can clearly be identified.

4. Cameras

Our criteria for selecting a camera suitable for synchrotron microtomography centered on the following: large active area of the chip but still useable with standard optics, small pixel size. Frequently this leads to CCD chips with an area similar to the 35-mm film and up to 10 megapixels resolution. The frequency response required is an efficiency above 40% between 400 nm and 800 nm. For optimal duty cycles a read-out speed of at least 1 FPS (frames per second) with a CCD's dynamic (full well capacity vs. read-out noise) of 12 bit or more is needed. Low thermal noise, linearity, no dead pixels have to be in agreement with common scientific grades [62].

Two CCD cameras are used for imaging at the BAM*line* (as we use two different optics this will allow us in principle an on-the-fly switching between both of them): Princeton Instruments *VersArray: 1300B* and *VersArray: 2048B*. The first uses an *E2V (Marconi) CCD36-40* chip (scientific grade 1) with 1340x1300 pixels – back-illuminated for a broad bandwidth and slow-scan for low read-out noise. The pixel size is 20 μm with a 100% fill factor. At the maximum read-out speed of 1 MHz the camera performs with a 16 bit dynamic range of 37500:1. The quantum efficiency is above 40% between 400 nm and 900 nm with a peak efficiency of above 90%. The second is a *VersArray: 2048B* with a 2048x2048 pixel CCD chip (*E2V (Marconi) CCD42-40*, 13.5 μm pixel size) and a 14 bit dynamic range of 11.111:1 at the maximum read-out speed of 1 MHz.

Both cameras have been chosen due to their excellent wavelength bandwidth, high dynamic range and frequency response which allows us to use a broad range of scintillating materials combined with all kinds of optics, even with low numerical apertures. The *VersArray: 1300B* fits the requirements of the macroscope (see section II C 2) with its moderate resolution. Due to the limited synchrotron beam height depending on the energy the camera works commonly with a field of view reduced to an electronically defined region-of-interest leading to read-out speeds of around 1 FPS with an excellent 16 bit dynamic range. At X-ray energies between 10 keV and 30 keV and moderate resolutions exposure times of approx. 1 s are required resulting in a duty cycle of around 50%. The *VersArray: 2048B* is used to achieve high resolution in combination with the microscope (section II C 3) and is usually operated without any region-of-interest. The resulting read-out time of 4 s is high but as exposure times, e.g. for resolutions between 1 μm and 2 μm, can go above 10 s at

the BAM*line* we still work with duty cycles around 50%. But still the slow read-out of the *VersArray: 2048B* can be improved in the future for example by replacing it with the ESRF's CCD camera FReLoN *2k14bit* [63].

A CMOS camera is under commissioning for fast radiography, preferable operated in white beam mode in order to work with an applicable high flux.

III. SYNCHROTRON MICROTOMOGRAPHY

For imaging with a contrast related only to the local X-ray attenuation coefficient of a specimen we use a distance between scintillator and sample of down to 5 mm (depending on the resolution), otherwise by means of phase contrast edge-enhancements will contribute to the contrast as well. Projection images at high resolution from many viewing angles are taken, the number of required projections is determined by the number of horizontal pixels in a row of the CCD or corresponding region-of-interest [64]. Conventional filtered backprojection [64] is performed by either PyHST (SciSoft group of the ESRF [65]) or a BAM in-house software package [5].

Due to the limited amount of photons available only the double multilayer monochromator (DMM) is used for microtomography at the BAM*line*: for example at 16 keV X-ray energy we can work with a flux of $6 \cdot 10^{10}$ Photons$\cdot$mm$^{-2}\cdot$s^{-1} (cf. fig. 2) at the position of the experiment (which is moderate compared to other insertion device beamlines at third generation storage rings [17, 18, 21, 38, 39]). Considering a typical microtomography pixel size of 1 μm (micrometer-resolution) and keeping in mind that thin scintillators are required for high resolution imaging [11] which lowers the detective quantum efficiency of our imaging system: one can estimate that up to 10 s exposure time per projection image are necessary in order to make use of the full dynamic range of our detector system (see also section II C). For a synchrotron microtomography scan with 3140 projections and the necessary bright-field images this means that a total exposure time of approx. 10 h is required (a tomography scan of a 1 mm thick silicon sample with these parameters would lead to a real spatial resolution of approx. 2 μm (considering Shannon's theorem [66]) and a material contrast of approx. 3.5% – higher resolutions are therefore only possible with lower contrast or exposure times $\gg$ 10 s [67]) which is already on the upper limit of an acceptable amount of beamtime necessary per scan. With less ambitious parameters like 2 μm pixel size and

1500 projections one would end up with a real spatial resolution of approx. 4 μm (Shannon's theorem) and a material contrast of approx. 2.4%, the required scan time for this case is around 1 h [67]. The DCM with up to two orders of magnitude less flux is therefore not suitable for microtomography at the BAM*line* and is only used for refraction enhanced imaging or Bragg magnification techniques (e.g. at an X-ray energy of 16 keV a flux density of $5 \cdot 10^8$ Photons$\cdot$mm$^{-2}\cdot$s^{-1} was measured when using the DCM while with the DMM $6 \cdot 10^{10}$ Photons$\cdot$mm$^{-2}\cdot$s^{-1} are available – for further details on the DCM see [13, 14]).

For highest resolutions available with the Optique Peter microscope (paragraph II C 3) the height of the field of view is approx. 1.4 mm (0.7 μm effective pixel size) or 0.7 mm (0.35 μm effective pixel size) which can be (depending on the energy used) significant smaller than the beam height. In order to overcome flux limitations which mainly means to reduce exposure times we use the bending option of the second mulitlayer of the DMM [14], resulting in a vertically focused beam and a reduction of the required exposure times by a factor of up to ten. In fig. 9 two scans of the horizontal line pairs of a Xradia test pattern (X500-200-30) can be seen, imaged using a 20x magnification (0.7 μm effective pixel size). The left image was recorded using maximal focusing, leading to a ten times shorter exposure time. The right image was captured with a non-focused beam, no change in resolution is visible when keeping the sample-detector distance small (5 mm, larger distances lead to a significant blurring) which is in agreement with results of other groups [68].

As an example for microtomography with moderate resolution using the macroscope described in section II C 2 fig. 10 shows tomographic images of a relatively large (12 mm horizontal diameter) specimen of sheep jawbone with implanted biodegradable ceramic particles [69]. The effective pixel size is 7 μm with a 14 mm x 14 mm field of view (27 keV X-ray energy, Gadox powder screen scintillator). In the radiographic projection the resolution was estimated to about 20 μm with the help of a copper knife-edge (10% of the MTF). A typical slice of this tomographic volume acquired is pictured on the left image of fig. 10 – ceramic particles can be recognized in light grey, the bone is grey and the remaining information the and pores. The ceramic particles can be separated due to their high contrast and well-defined morphology. A 3D rendering of the fully segmented volume image is shown in the right image of fig. 10.

In fig. 11 high resolution tomographic slices of a fibre reinforced C/SiC ceramic (Fraunhofer ISC, Dr. J. Meinhardt) are depict (9x and a 21x magnification – section II C 3). A scan

with a field of view of 3 mm x 3 mm and resulting resolution of < 4 μm (10% of the MTF, 17 keV X-ray energy, 1.5 μm pixel size, CWO scintillating single crystal) reveals the silicon (light gray) and the carbon phase (dark). The latter has a substructure due to the fibres, silicon-carbon SiC crystals are visible at the inferface due to edge enhancement (as verified by comparing with SEM investigations, see [43]). Scanning the same sample region with a higher resolution (< 2 μm as determined via a Siemensstar, 0.6 μm effective pixel size, 17 keV X-ray energy, LuAG:Eu scintillating single crystal 4 μm thick) and a corresponding smaller field of view (local tomography [64], here with remarkable nearly zero artifacts) provides further detail information: single SiC crystals are discernible, and single carbon fibres as well as micro-cracks can be identified [43].

IV. PHASE CONTRAST AND HOLOTOMOGRAPHY

For direct imaging techniques the interaction of X-rays with a given material is described by the complex refractive index n which is almost unity:

$$n = 1 - \delta + i\beta \tag{2}$$

While standard X-ray absorption images show a projection of the imaginary part β – mostly accounted to the photoelectric effect – the real decrement δ remains inaccessible unless Fresnel-propagation is used. Measurements of δ constitute a great advantage as it can be up to three orders of magnitude larger than β for certain materials and energies. X-ray imaging based on Fresnel-propagation has been employed to image the contribution of both parameters for more than a decade [22–24, 70]. The visibility of interfaces and sub-micrometer features is enhanced in the images by simply increasing the sample-to-detector distance by a few centimeters. Fig. 12 shows a series of images taken from two hairs at increasing sample-to-detector distances. Such weakly absorbing objects do not appear at all in absorption contrast images because of their negligible X-ray attenuation (Fig. 12 – left). With increasing propagation distances (up to one meter) not only the outline of the hairs but also details of the biological microstructure become visible. These images were recorded at E = 20 keV photon energy using a LuAG:Eu scintillator screen and optics resulting in an effective pixel size of 0.6 μm (resolution < 2 μm as determined via a Siemensstar). Fresnel-propagation can be combined with tomography in order to record three-dimensional

structure that would not appear in absorption images. For structural details of the order of 1 μm the interference pattern spreads beyond the dimensions of the features, consequently we can see details which are below the resolution of a given detector system [71].

It has been shown that using the Guigay approximations [72] one can combine a series of Fresnel-propagated radiographs in order to retrieve a projection image of the real decrement δ, which corresponds to the electron density of the material. Combining this phase retrieval with tomography, thus processing to holotomography, we are able to investigate structure of phase objects (such as biological materials that have to be investigated at high X-ray energies) or discern material phases that have similar absorption coefficients and therefore appear as one homogeneous material in absorption images.

An example for such a material is shown in fig. 13. The magnesium-aluminum alloy AZ91 is mainly a binary mixture of two phases with similar refractive indices. Imaging the real part yields an absorption tomogram with insufficient material contrast (cf. fig. 13 – left). Increasing the sample-to-detector distance results in fig. 13 (middle) with enhancement of the structural interfaces. We used a method based on contrast transfer functions in order to retrieve the phase maps (projection images of δ) from a set of four tomographic scans recorded at D = 15 mm, 144 mm, 433 mm and 720 mm, then compute the holo-tomogram, a slice of which is shown in fig. 13 – right. The X-ray energy used for these images was E = 23 keV, 900 radiographic projections were recorded at each propagation distance with an effective pixel size of 1.6 μm (resolution < 4 μm, 10% of the MTF) using a CWO single crystal scintillating screen.

V. SYNCHROTRON REFRACTION ENHANCED TOMOGRAPHY

Synchrotron refraction enhanced tomography is a promising tool to reveal the changes and development of inner surfaces (e.g. fibre matrix interfaces) of high performance composites, ceramics and other advanced materials, which show anisotropy, heterogeneity and complex shapes [27, 58]. X-ray refraction reveals the inner surfaces and interface concentrations of nanometer dimensions due to the short X-ray wavelength near 0.1 nm [73, 74]. Particles with submicrometer size, cracks and pore sizes are easily determined by X-ray refractometry without destroying the structure by cutting or polishing for microscopic techniques. The physics of X-ray refraction is quite similar to the well known refraction of the visible light

by optical lenses and prisms, which is governed by Snell's law. However, a major feature compared to optics of visible light is, that the refractive index n of X-rays in matter is nearly unity ($n < 1$). This causes deflections at very small angles in the order of a few minutes of arc. A more detailed description of the refraction enhanced imaging method has recently been published [74]. The technique requires an elaborate experimental setup, which has been outlined in section II B.

To perform the measurement a parallel monochromatic beam (up to 60 keV) from the DMM (or the DCM) with a band width of about 1.7% (or 0.2%) is used. The beam is reflected by two Si(111) single crystals in a symmetric configuration. They are set to their Bragg angles (at the maximum of the Rocking Curve) for the relevant energy. The X-ray sensitive camera (macroscope, see section II C 2) system is placed downstream of the second crystal and detects the photons reflected by this crystal. The Rocking Curve of the crystal pair can be recorded by tilting the second crystal against the first crystal around the Bragg angle while measuring the reflected intensity. The width of the Rocking Curve for Si(111) at 50 keV is FWHM = $3.9{\cdot}10^{-4}$ deg (1.404 arcsec, cf. fig. 14 – open circles). The sample is positioned in the X-ray beam between the two crystals in the goniometer. The highly collimated and monochromatized beam from the first crystal traverses the specimen and is attenuated due to the specimen's absorption properties. Additionally, X-rays are deflected at all interfaces in the sample due to refraction. This leads to a broadening of the Rocking Curve as shown in fig. 14 to FWHM = $4.9{\cdot}10^{-4}$ deg (1.764 arcsec, cf. fig. 14 – filled circles). As a consequence, all X-rays scattered at angles larger than the rocking curve are stopped by the second crystal, if the crystal pair is set to its Rocking Curve maximum. This is illustrated in fig. 5 and 14. The refracted X-rays from the inner surfaces of the sample are blocked by the second crystal. The result is a significant contrast enhancement in the radiographic projection image of the sample. If the second crystal is slightly off the Rocking Curve maximum only the scattered X-rays will be reflected and detected by the camera.

We illustrate the high potential of this method by imaging a cylindrical reinforced fibre specimen (MTU Aero Engines). The reinforcing fibre was Textron's SCS6-fibre. The sample contains a 33 μm diameter carbon fibre as a core with a 1 μm pyro-C-protective coating, followed by SiC and again by a pyro-C-protective coating of 3 μm. The overall diameter of the fibre measures 140 μm. The fibres are sputtered (30 μm) with a titanium based alloy Ti6242 and are bundled and formed by Hot Isostatic Pressing. Static and cyclic loading was

applied to the fibres in order to obtain the values of several mechanical parameters. As a new approach for non-destructive testing the specimens were investigated at the BAM*line* with refraction enhanced tomography. The measurements were performed by rotating the specimens around their cylinder axis for 360 degrees in steps of 1 degree. The data sets were reconstructed by the filtered back projection as known from the data treatments for conventional absorption CT [5, 64].

Fig. 15 (left) shows the reconstruction of one cross section of the sample from an absorption data set, obtained with a BAM in-house laboratory CT (100 kV, 4.7 μm effective pixel size [9]). The reinforcing SiC-fibres show up as discs in the titanium matrix (main area). The fibres are not symmetrically arranged with respect to the rotational axis of the specimen. A crack is seen on the right hand side of the cross section, which corresponds very well to the visible crack in the cladding of the specimen. No further indications can be seen for cracks or fibre failure in the remaining area. Fig. 15 (right) demonstrates the power of refraction enhanced tomography. Data were acquired on the BAM*line* using 50 keV, 5.3 μm effective pixel size. By comparison to the figure on the left, many more details are seen. The absorption information is the same, but in addition the refraction effect reveals, that the crack distribution in the matrix is vaster than determined from the absorption information.

VI. MAGNIFICATION BY ASYMMETRIC BRAGG REFLECTION

One approach to overcome the limitations mentioned in section II C and to achieve true submicrometer resolution is the use of asymmetric Bragg reflections in front of the detector system. The method is based on the use of asymmetric cut Bragg crystals where the crystal surface is inclined by an asymmetry angle against the reflecting lattice planes (see fig. 16). A resolution of about 0.5 μm was already reported by Förster et al. [75]. A magnification in two dimensions by use of two asymmetric Bragg reflections was realized by Köhler et al. [76]. According to the equation given in fig. 16, the magnification can by varied up to a factor of 100 or even more by simply changing the photon energy. A two-dimensional submicrometer resolution can be achieved just as well by combining the Bragg magnification with the CT technique (see fig. 5) by replacing the analyser crystal by an asymmetric cut Bragg crystal (crystals providing a magnification of a factor of 20 at 10 keV, 20 keV, 30 keV and 40 keV are furnished).

As an example we show a stainless steel micro drill (100 μm diameter, 1 mm length) measured at 19 keV photon energy. The magnification plane was perpendicular to the axis of rotation. Fig. 17 shows the reconstruction of a sagittal and an axial section of the drill. In the sagittal plane, the vertical pixel size is about 5.6 μm while in the horizontal pixel size is about 150 nm. In the axial plane the two-dimensional pixel size is about 150 nm. Tubular pores with dimensions below 1.0 μm diameter can be resolved (cf. fig. 18). In addition the refraction enhanced contrast at the outer edges and around the pores is visible.

VII. SUMMARY

In this article we have introduced the high resolution synchrotron-based radiography and tomography setup at the BAM*line* (BESSY II), suitable to investigate specimens, in a non-destructive manner, with resolutions up to 1.0 μm (as verified with a Xradia test pattern) and contrast modes measuring the local attenuation coefficient (synchrotron microtomography), the local electron density (holotomography) and inner surfaces and interfaces (refraction enhanced tomography). True submicrometer resolution is achieved by using asymmetric Bragg reflections as a beam width magnifier, demonstrated via imaging submicrometer sized tubular pores in a stainless steel micro drill. The high potential of this device is illustrated by investigations of specimens originating from life science (bioregenerating bone tissue), materials research (commercial magnesium-aluminum thixo-alloy AZ91) and non-destructive testing (fibre reinforced samples). Various optimization approaches such as using a focused synchrotron beam or a dedicated scintillator concept have been tested successfully, resulting in a higher performance of our setup. Future further improvements include new scintillator development with materials such as GGG:Eu [50], LuAG:Ce [77] and specially LSO:Tb [78]. Other forms of imaging, including white beam and methods with dual energy imaging have shown promising results as well.

Acknowledgments

We acknowledge C. David (PSI) for supplying different test patterns and gratings, T. Martin, P. Cloetens (ESRF), L. Helfen, T. Weitkamp (ANKA), P. Zaslansky (MPG), F. De Carlo (APS) for all the fruitful discussions, K. Dupre, A. Ackermann (FEE GmbH) for the

countless informations on single crystals, A. Haibel (HMI) for administrative support, L. Nagornaya, V. Ryzhikov (STRCI – STC "Institute for Single Crystals") for providing CWO single crystals, J. Meinhardt (Fraunhofer ISC) for the fibre reinforced C/SiC ceramic, M. Stiller, C. Knabe (Charité Berlin) for various tissue specimens of regenerated bone, T. Wolk, M. Klinger, H. Heimbach (BAM) for various constructions and excellent technical support. Special thanks to Tatjana!

---

[1] W. C. Röntgen. Über eine neue Art von Strahlen. In secretary of the Physical-Medical Society, Würzburg (1895).

[2] A. M. Cormack. J. Appl. Phys. **34** (9) (1963) 2722-2727.

[3] G. N. Hounsfield. Brit. J. Radiol. **46** (552) (1973) 1016-1022.

[4] J. Hsieh. *Computed Tomography – Principles, Design, Artifacts and Recent Advances.* SPIE Press (2003).

[5] P. Reimers, J. Goebbels. Mat. Eval. **41** (6) (1983) 732-737.

[6] J. Banhart (Ed.). *Advanced Tomographic Methods in Materials Research and Engineering.* Oxford University Press, Oxford (2007).

[7] B. P. Flannery, H. W. Deckmann, W. G. Roberge, K. L. D'Amico. Science **237** (4821) (1987) 1439-1444.

[8] U. Bonse, F. Busch. Prog. Biophys. Molec. Biol. **65** (1) (1996) 133-169.

[9] J. Goebbels, B. Illerhaus, Y. Onel, H. Riesemeier, G. Weidemann. 3D-Computed Tomography over four Order of Magnitude of X-Ray Energies. Proc. 16th World Conference on Nondestructive Testing – WCNDT2004. `www.ndt.net/article/wcndt2004/pdf/radiography/559_goebbels.pdf`

[10] W. Graeff, K. Engelke. Microradiography and Microtomography. In *Handbook on Synchrotron Radiation Volume 4*, ed. S. Ebashi, M. Koch, E. Rubenstein, North-Holland, Amsterdam; Oxford; New York; Tokyo (1991).

[11] A. Koch, C. Raven, P. Spanne, A. Snigirev. J. Opt. Soc. Am. **15** (7) (1998) 1940-1951.

[12] R. J. Bakker. Status and commissioning – results of BESSY II. Proc. of the IEEE Particle Accelerator Conference, Vol. 1, 197-199, 1999.

[13] W. Görner, M. P. Hentschel, B. R. Müller, H. Riesemeier, M. Krumrey, G. Ulm, W. Diete, U.

Klein, R. Frahm. Nucl. Instr. Meth. A **467** (2001) 703-706.

[14] H. Riesemeier, K. Ecker, W. Görner, B. R. Müller, M. Radtke, M. Krumrey. X-Ray Spectr. **34** (2005) 160-163.

[15] G. Weidemann, J. Goebbels, Th. Wolk, H. Riesemeier. First Computed Tomography Experiments at BAM*line*. BESSY Annual Report 2001, 249-250.

[16] J. Baruchel, J.-Y. Buffiere, P. Cloetens, M. Di Michiel, E. Ferrie, W. Ludwig, E. Maire, L. Salvo. Scripta Mat. **55** (2006) 41-46.

[17] M. Stampanoni, G. Borchert, P. Wyssc, R. Abela, B. Patterson, S. Hunt, D. Vermeulen, P. Rüegsegger. Nucl. Instr. & Meth. A **491** (2002) 291-301.

[18] F. Beckmann, T. Lippmann, J. Metge, T. Dose, T. Donath, M. Tischer, K. D. Liss, A. Schreyer. HARWI-II, The New High-Energy Beamline for Materials Science at HASYLAB/DESY. SRI 2003 – AIP Conference Proc. Vol. 708, 392-395, 2004.

[19] K. Uesugi, Y. Suzuki, H. Takano, S. Tamura, N. Kamijo, N. Yagi. Direct Measurement of the Resolving Power of X-ray CT System in SPring-8. SRI 2003 – AIP Conference Proc. Vol. 708, 1316-1319, 2004.

[20] H.-R. Lee, B. Lai, W. Yun, D. C. Mancini, Z. Cai. X-ray Microtomography as a Fast Three-Dimensional Imaging Technology Using a CCD Camera Coupled with a CdWO4 Single-Crystal Scintillator. Proc. of SPIE Vol. 3149, 257-264, 1997.

[21] Y. Wang, F. De Carlo, D. C. Mancini, I. McNulty, B. Tieman, J. Bresnahan, I. Foster, J. Insley, P. Lange, G. von Laszewski, C. Kesselmann, M.-H. Su, M. Thibaux. Rev. Sci. Instr. **72** (4) (2001) 2062-2068.

[22] A. Snigirev, I. Snigireva, V. Kohn, S. Kuznetsov. Rev. Sci. Instr. **66** (12) (1995) 5486-5492.

[23] P. Cloetens, R. Barrett, J. Baruchel, J.-P. Guigay, M. Schlenker. J. Phys. D: Appl. Phys. **29** (1) (1996) 133-146.

[24] K. A. Nugent, T. E. Gureyev, D. F. Cookson, D. Paganin, Z. Barnea. Phys. Rev. Lett. **77** (1996) 2961-2964.

[25] P. Cloetens, W. Ludwig, J. Baruchel, D. Van Dyck, J. Van Landuyt, J. P. Guigay, M. Schlenker. Appl. Phys. Lett. **75** (19) (1999) 2912-2914.

[26] A. W. Stevenson, T. E. Gureyev, D. Paganin, S. W. Wilkins, T. Weitkamp, A. Snigirev, C. Rau, I. Snigireva, H. S. Youn, I. P. Dolbnya, W. Yun, B. Lai, R. F. Garrett, D. J. Cookson, K. Hyodo, M. Ando. Nucl. Instr. & Meth. B **199** (2003) 427-435.

[27] B. R. Müller, A. Lange, M. Harwardt, M. P. Hentschel, B. Illerhaus, J. Goebbels, J. Bamberg, F. Heutling. First Refraction Enhanced 3D Computed Tomography. Proc. of the International Symposium on Computed Tomography and Image Processing for Industrial Radiology, ed. J. Goebbels and U. Zscherpel (DGZfP Proceedings BB 84-CD, ISBN 3-931381-48-X), 2003.

[28] P. Cloetens. Contribution to Phase Contrast Imaging, Reconstruction and Tomography with Hard Synchrotron Radiation. Dissertation, Vrije Universiteit Brussel, 1999.

[29] M. Born, E. Wolf. *Principles of Optics.* 7. (extended) edition, Cambridge University Press (1999).

[30] J. P. Guigay. Opt. Acta **18** (9) (1971) 677-682.

[31] J. P. Guigay, S. Zabler, P. Cloetens, C. David, R. Mokso, M. Schlenker. J. Synchrotron Rad. **11** (6) (2004) 476-482.

[32] T. Weitkamp, B. Nöhammer, A. Diaz, C. David. Appl. Phys. Lett. **86** (2005) 54101.

[33] B. R. Müller, M. P. Hentschel. X-Ray Spectr. **33** (2004) 402-406.

[34] M. Eichelbaum, K. Rademann, R. Müller, M. Radtke, H. Riesemeier, W. Görner. Angew. Chemie **44** (48) (2005) 7905-7909.

[35] W. Görner, R. Matschat, M. Radtke, U. Reinholz, H. Riesemeier, M. Eichelbaum, K. Rademann. Insight – Non-Destructive Testing and Condition Monitoring **48** (9) (2006) 540-544.

[36] M. Krumrey, M. Gerlach, F. Scholze, G. Ulm. Nucl. Instr. & Meth. in Phys. Res. A **568** (2006) 364-368.

[37] L. Büermann, B. Grosswendt, H.-M. Kramer, H.-J. Selbach, M. Gerlach, M. Hoffmann, M. Krumrey. Phys. Med. Biol. **51** (2006) 5125-5150.

[38] K. Uesugi, Y. Suzuki, N. Yagi, A. Tsuchiyama, T. Nakano. Development of sub-micrometer resolution x-ray CT system at SPring-8. Proc. of SPIE Vol. 5003, 291-298, 2002.

[39] T. Weitkamp, C. Raven, A. A. Snigirev. Imaging and microtomography facility at the ESRF beamline ID 22. Proc. of SPIE Vol. 3722, 311-317, 1999.

[40] G. Weidemann, J. Goebbels, H. Riesemeier, Th. Wolk. Computed tomography experiments at BAM*line*. BESSY Annual Report 2004, 481-482.

[41] R. K. Swank. Appl. Optics **12** (8) (1973) 1865-1870.

[42] T. Martin, A. Koch. J. Synchrotron Rad. **13** (2006) 180-194.

[43] A. Rack. PhD thesis – Technical University Berlin 2006. `http://opus.kobv.de/tuberlin/volltexte/2006/1370`

[44] M. Tanaka, O. Harada. (*in Japanese*) Mazda Research Report **8** (1933) 167.

[45] C.-C. Glüer, W.-R. Dix, K. Engelke, W. Graeff, W. Kupper, K.-H. Stellmaschek. Med. Phys. **16** (1) (1989) 98-104.

[46] F. Beckmann, T. Donath, T. Lippmann, A. Schreyer, H. Clemens. Synchrotron-radiation based microtomography of new materials for lightweight construction. Proc. of the International Symposium on Computed Tomography and Image Processing for Industrial Radiology, ed. J. Goebbels and U. Zscherpel (DGZfP Proceedings BB 84-CD, ISBN 3-931381-48-X), 2003.

[47] L. Nagornaya, G. Onyshchenko, E. Pirogov, N. Starzhinskiy, I. Tupitsyna, V. Ryzhikov, Y. Galich, Y. Vostretsov, S. Galkin, E. Voronkin. Nucl. Instr. & Meth. in Phys. Res. A **537** (1-2) (2005) 163-167.

[48] H. Murayama, E. Tanaka, N. Nohara, T. Tomitani, M. Yamamoto, T. Hayashi. Nucl. Instr. & Meth. in Phys. Res. A **221** (3) (1984) 633-640.

[49] A. Koch, F. Peyrin, P. Heurtier, B. Ferrand, B. Chambaz, W. Ludwig, M. Couchaud. X-ray camera for computed microtomography of biological samples with micrometer resolution using $Lu_3Al_5O_{12}$ and $Y_3Al_5O_{12}$ scintillators. Proc. of SPIE Vol. 3659, 170-179, 1999.

[50] T. Martin, M. Couchaud, B. Ferrand, A. Caillet, D. Pelenc, B. Chambaz, A. Passero. Thin-film scintillators for computed microtomography with micrometer resolution using $Gd_3Ga_5O_{12}$ scintillators. Proc. 8th International Conference on Inorganic Scintillators and their Applications – SCINT2005.

[51] C. L. Melcher, J. S. Schweitzer. IEEE Transactions on Nuclear Science **39** (4) (1992) 502-505.

[52] R. Nutt, C. L. Melcher. Revue de l'ACOMEN **5** (2) (1999) 152-155.

[53] I. G. Valais, I. S. Kandarakis, A. Konstantinidis, D. N. Nikolopoulos, I. Sianoudis, D. A. Cavouras, N. Dimitropoulos, C. D. Nomicos, G. S. Panayiotakis. Nucl. Instr. Meth. A **569** (2) (2006) 201-204.

[54] Rodenstock – X-Ray Manual (catalogue) former Optische Werke G. Rodenstock – Precision Optics Division, now: Linos AG.

[55] H. H. Hopkins. Proc. R. Soc. London, Ser. A **231** (1955) 91-103.

[56] S. Zabler, K. Thermann, B. Kremmin, H. Riesemeier, I. Manke, A. Rack, J. Tiedemann. Three-dimensional analysis of hard rock: from micro porosity to the footprint of a macro crack. Journal of Structural Geology (submitted, 2006).

[57] A. Rack, A. Haibel, A. Bütow, B. Matijašević-Lux, J. Banhart. Characterization of metal

foams with synchrotron-tomography and 3d image analysis. Proc. 16th World Conference on Nondestructive Testing – WCNDT2004. www.ndt.net/article/wcndt2004/pdf/materials_characterization/370_rack.pdf

[58] J. Goebbels, B. R. Müller, H. Riesemeier, G. Weidemann. Special Solutions for CT-Investigations with Synchrotron Radiation. Proc. NDT in Progress (ISBN 80-214-2475-3), 91-97, 2003.

[59] C. G. Schroer, B. Benner, T. F. Günzler, M. Kuhlmann, J. Patommel, B. Lengeler, A. Somogyi, T. Weitkamp, C. Rau, A. Snigirev, I. Snigireva. Proc. of SPIE Vol. 5535, 701-708, 2004.

[60] T. Weitkamp, A. Rack, L. Helfen, T. Baumbach. The future IMAGE beamline at ANKA. Poster presentation, 9th International Conference on Synchrotron Radiation Instrumentation – SRI2006.

[61] V. Babin, K. Blažek, A. Krasnikov, K. Nejezchleb, M. Nikl, T. Savikhina, S. Zazubovich. phys. stat. sol. **2** (1) (2005) 97-100.

[62] S. M. Gruner, M. W. Tate, E. F. Eikenberry. Rev. Sci. Instr. **73** (8) (2002) 2815-2842.

[63] J.-C. Labiche, O. Mathon, S. Pascarelli, M. A. Newton, G. G. Ferre, C. Curfs, G. Vaughan, A. Homs, D. F. Carreiras. Rev. Sci. Instrum. **78** (2007) 0901301-0901311.

[64] A. C. Kak, M. Slaney. *Principles of Computerized Tomographic Imaging.* IEEE Press, New York (1988).

[65] A. Mirone, R. Wilcke, A. Hammersley, C. Ferrero. PyHST – High Speed Tomographic Reconstruction. www.esrf.eu/UsersAndScience/Experiments/TBS/SciSoft – last visit july 2007.

[66] C. E. Shannon, W. Weaver. *Mathematical Theory of Communication.* University of Illinois Press, 1963.

[67] R. A. Brooks, G. DiChiro. Med. Phys. **3** (1976) 237-240.

[68] Y. Wang, S. Narayanan, J. Liu, D. Shu, A. Mashayekhi, J. Qian, J. Wang. J. Synchrotron Rad. **14** (2007) 138-143.

[69] A. Rack, C. Knabe, M. Stiller, Ch. Koch, H. Seligmann, S. Zabler, G. Weidemann, J. Goebbels. Synchrotron-Tomography for Evaluation of Bone Tissue Regeneration using rapidly Resorbable Bone Substitute Materials. Proc. 9th European Conference on Nondestructive Testing – ECNDT2006 (DGZfP Proceedings BB 103-CD, ISBN 3-931381-86-2). www.ndt.net/article/ecndt2006/doc/Th.1.2.2.pdf

[70] S. Zabler, P. Cloetens, J.-P. Guigay, J. Baruchel, M. Schlenker. Rev. Sci. Instr. **76** (7) (2005) 1-7.

[71] S. Zabler, H. Riesemeier, P. Fratzl, P. Zaslansky. Optics Express **14** (19) (2006) 8584-8597. `www.opticsinfobase.org/abstract.cfm?URI=oe-14-19-8584`

[72] J. P. Guigay. Optik **49** (1977) 121-125.

[73] A. H. Compton, S. K. Allison. X-ray in theory and experiment. D. van Nostrand Co., New York (1935).

[74] B. R. Müller, A. Lange, M. Harwardt, M. P. Hentschel, B. Illerhaus, J. Goebbels, J. Bamberg, F. Heutling. X-Ray Refraction Topography and Computed Tomography for NDE of lightweight materials. Proc. of SPIE Vol. 5766, 1-8, 2005.

[75] E. Förster, K. Goetz, P. Zaumseil. Kristall und Technik **15** (1980) 937-945.

[76] P. Schäfer, R. Köhler. J. Phys. D: Appl. Phys. **36** (2003) A113-A117.

[77] M. Nikl, E. Mihoková, J. A. Mareš, A. Vedda, M. Martini, K. Nejezchleb, K. Blažek. phys. stat. sol (a) **181** (2000) R10-R12.

[78] A. Rack, T. Martin, M. Couchaud, P.-A. Douissard, A. Cecilia, A. Danilewsky, T. Baumbach. Thin LSO-based mixed-crystal grown by liquid phase epitaxy for high resolution X-ray imaging. Poster presentation, 9th International Conference on Inorganic Scintillators and their Applications – SCINT2007.

[79] F. Schäfers, M. Krumrey. REFLEC. Program to Calculate VUV/X-ray Optical Elements and Synchrotron Radiation Beamlines. BESSY TB 201/96 (1996).

[80] M. S. del Río, R. J. Dejus. XOP: Recent Developments. Proc. of SPIE Vol. 3448, 340-345, 1998.

[81] S. Zabler, A. Rueda, A. Rack, A. Haibel, H. Riesemeier, J. Goebbels, T. Wolk, G. Weidemann, J. Banhart. Study of the Evolution of Semi-Solid Alloys By Means of Phase-Sensitive Synchrotron Tomography. Proc. 9th European Conference on Nondestructive Testing – ECNDT2006 (DGZfP Proceedings BB 103-CD, ISBN 3-931381-86-2). `www.ndt.net/search/pdf2html.php?url=article/ecndt2006/doc/We.1.5.2.pdf`

APPENDIX A: FIGURES

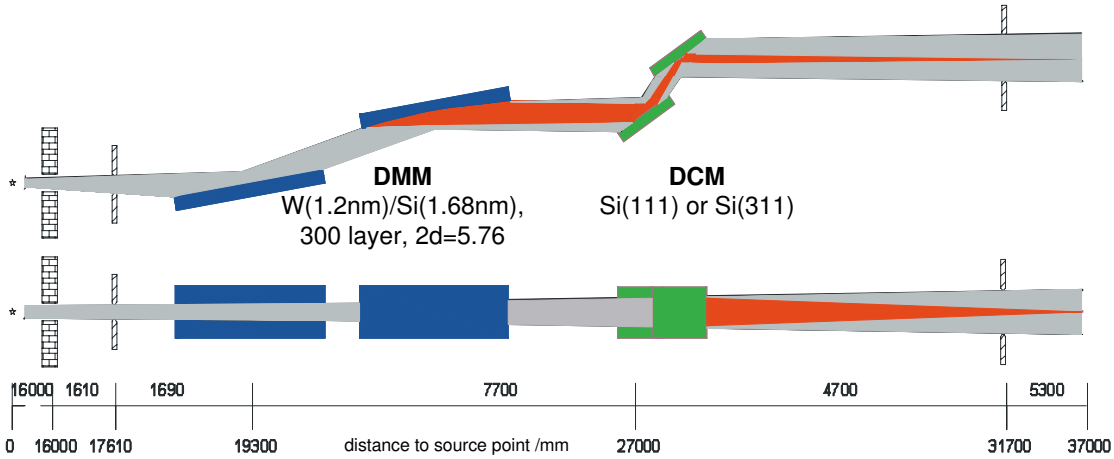

FIG. 1: Layout of the X-ray beampath at BAM*line* (top: side view, bottom: top view). The radiation originating from a 7T superconducting wavelength shifter can be monochromatized using a double multilayer monochromator (DMM) and/or a double crystal monochromator (DCM), including a vertical focusing option for the DMM and a horizontal for the DCM. The position of the tomography stage is in the experimental hutch at a distance of 35 m from the source [13, 14]. **print: BW, web: color**

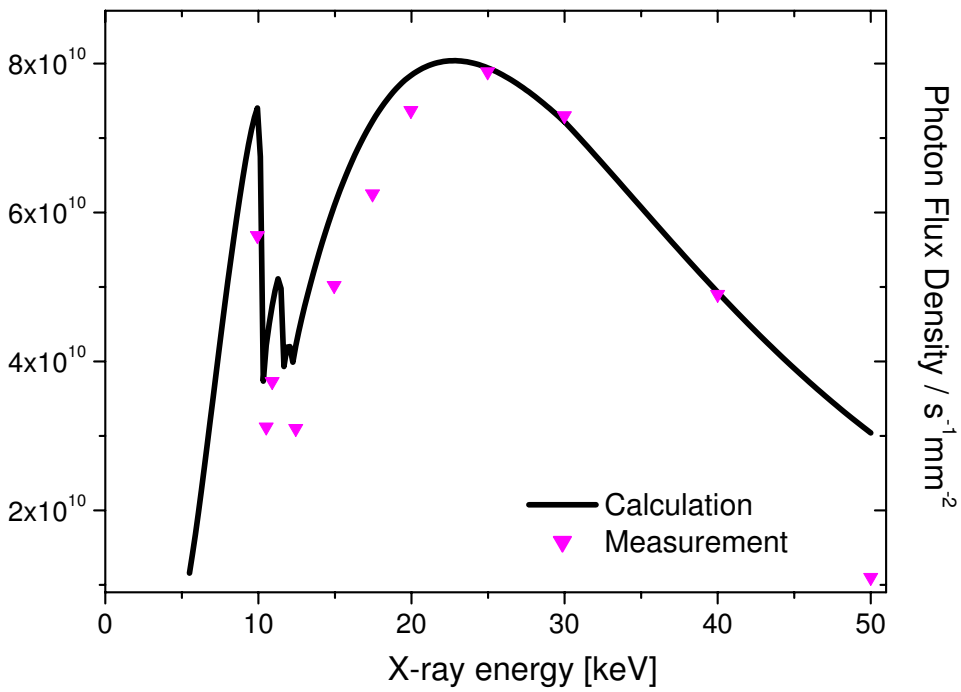

FIG. 2: Photon flux density behind the double multilayer monochromator at the BAM*line*; measured and calculated (using Reflec [79]) with a ring energy of 1.7 GeV, a ring current of 200 mA, a magnetic field of 7 T at the wavelength shifter insertion device and a distance from the source of 35 m. At 7 keV a flux density of 5.7x10^{10} Photons·mm^{-2}·s^{-1} was measured with a focused beam. Around 11 keV typical flux reduction due to the tungsten L absorption edges can be seen (the multilayer coating consists of 150 double layers W/Si).

print: BW, web: color

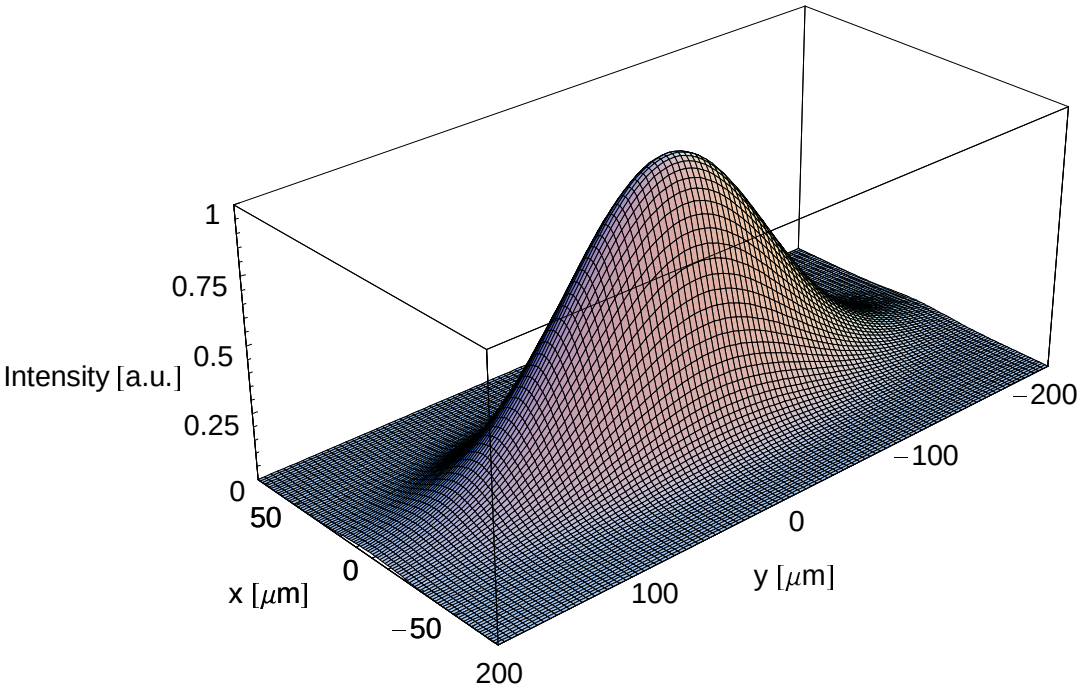

FIG. 3: The shape of the effective source intensity distribution at the BAM*line* as derived by Talbot imaging.

print: BW, web: color

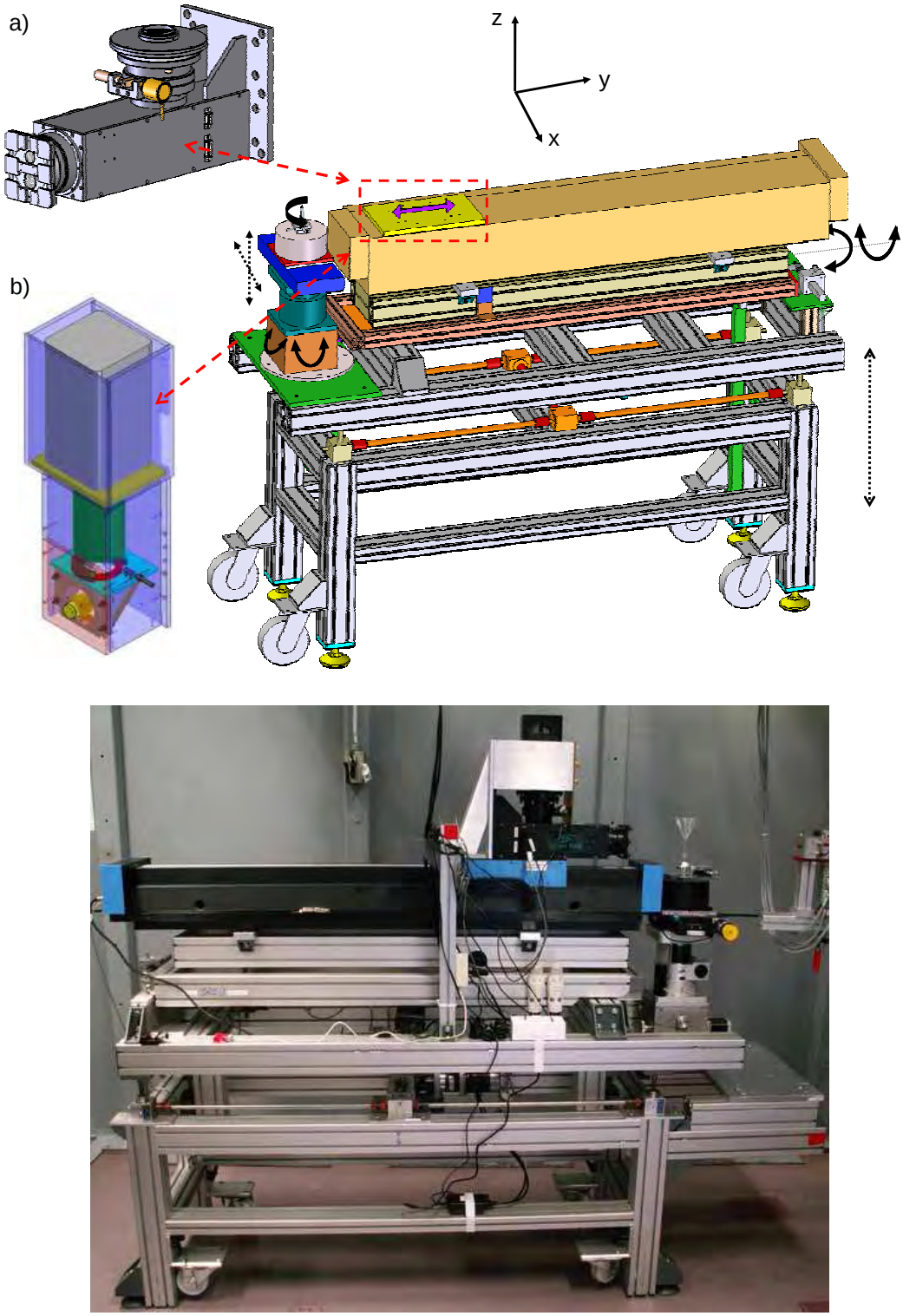

FIG. 4: Top: Sketch of the imaging setup at the BAM*line* with the sample manipulators mounted together with an airbeared stage (1.1 m travel-range) for the X-ray imaging detector (either a) microscope or b) macroscope) onto a table which is adjustable along the beam. The beam itself propagates in positive y-direction. Bottom: photo of setup with mounted microscope.

print: BW, web: color

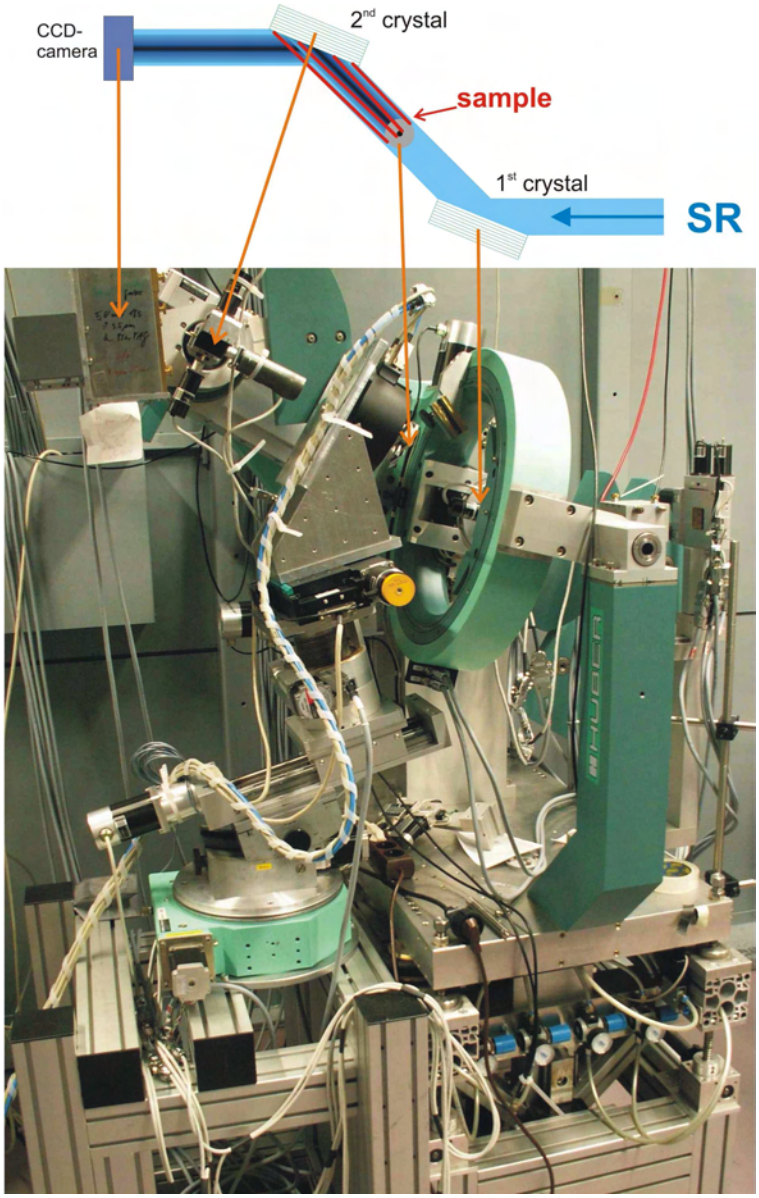

FIG. 5: Top: sketch of the experimental setup for refraction enhanced imaging – the rays of the monochromatic beam refracted by the sample are blocked by the second crystal. Bottom: photograph of the experimental setup. The 6-circle goniometer on the right carries the crystals and the camera system. The table on the left carries the sample manipulation stage.

print: BW, web: color

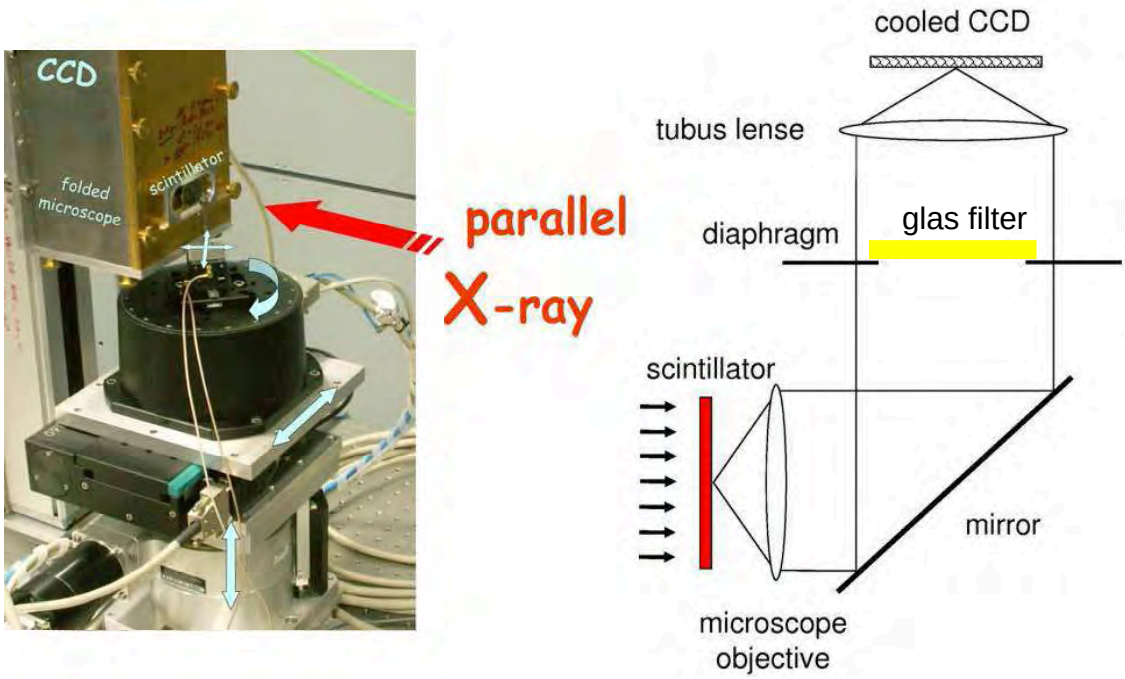

FIG. 6: Left: photo of the aligned macroscope at the BAM*line* with sample manipulator [15] and right: principle sketch of the X-ray imaging detector following the concepts of Busch and Bonse [8] with additional glas filters and a diaphragm in the beam path of the visible light.

print: BW, web: color

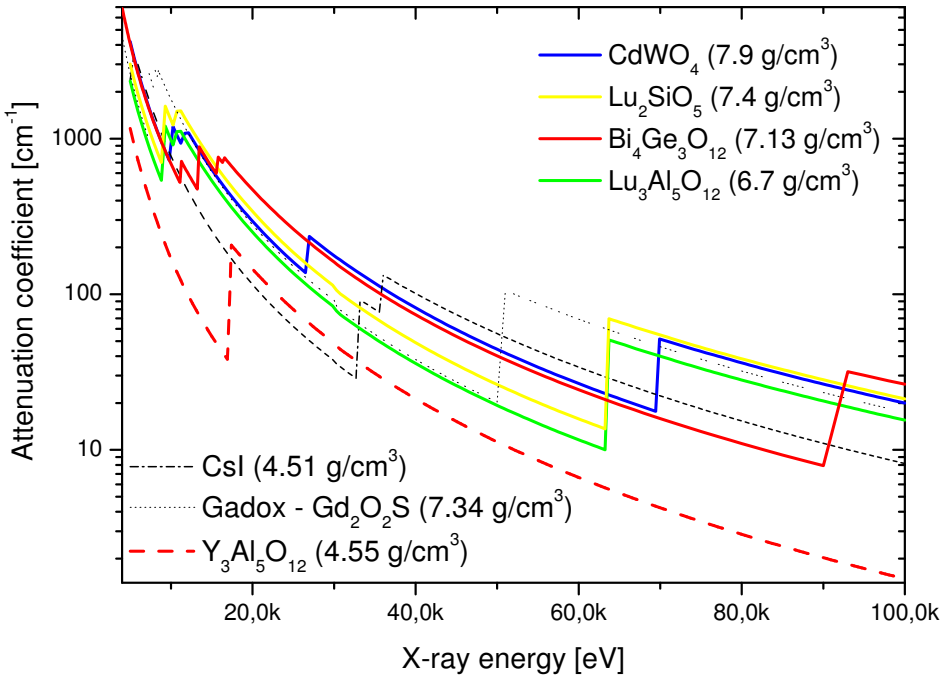

FIG. 7: X-ray attenuation coefficient of the (undoped) scintillating materials used at BAM*line* and that in medicine widely applied CsI with corresponding densities, calculated with Xop [80].

print: BW, web: color

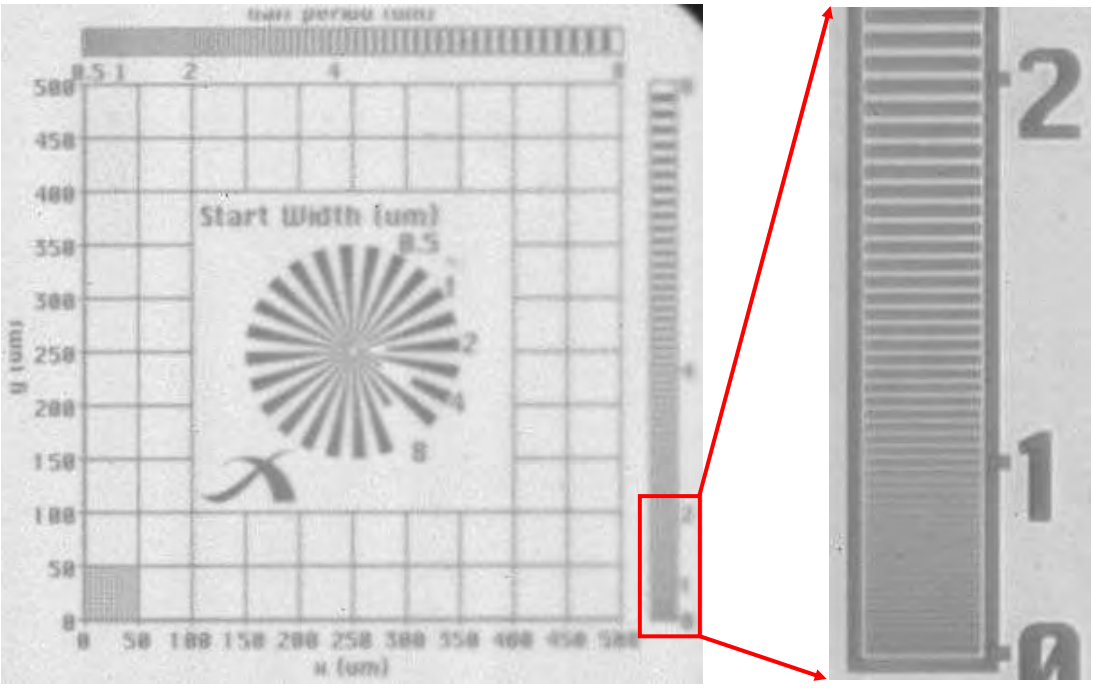

FIG. 8: Left: overview image of a Xradia test pattern (X500-200-30) done at BAM*line* using the microscope with an effective pixel size of 1.7 μm and a 40 μm thick CWO scintillating single crystal (15 keV X-ray energy), right: vertical line pattern with line sizes from 2 μm down to 0.5 μm imaged with highest resolution (0.35 μm effective pixel size, 40x magnification, LuAG:Eu scintillator 4 μm thick, 15 keV X-ray energy) – features smaller 1 μm are distinguishable, the distance sample to detector was 5 mm.

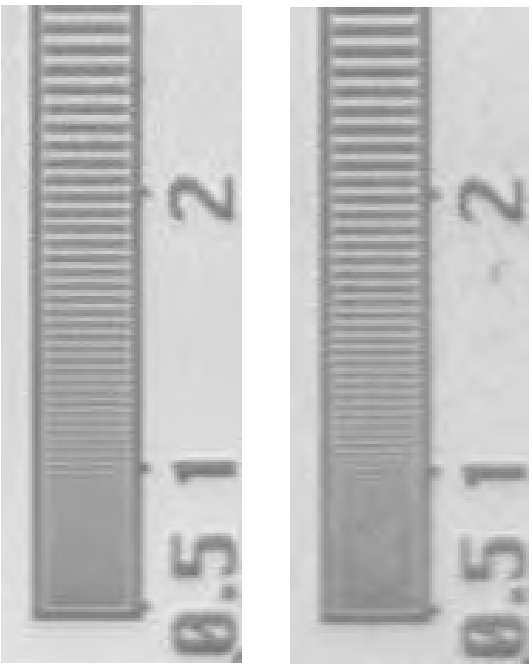

FIG. 9: Left: image of line pairs from a Xradia test pattern (X500-200-30) taken with 0.7 μm effective pixel size and a maximal vertical focused beam, right: same section imaged with a non-focused beam, no change in resolution is detectable, the distance sample to detector was 5 mm (15 keV photon energy, LuAG:Eu scintillator 4 μm thick).

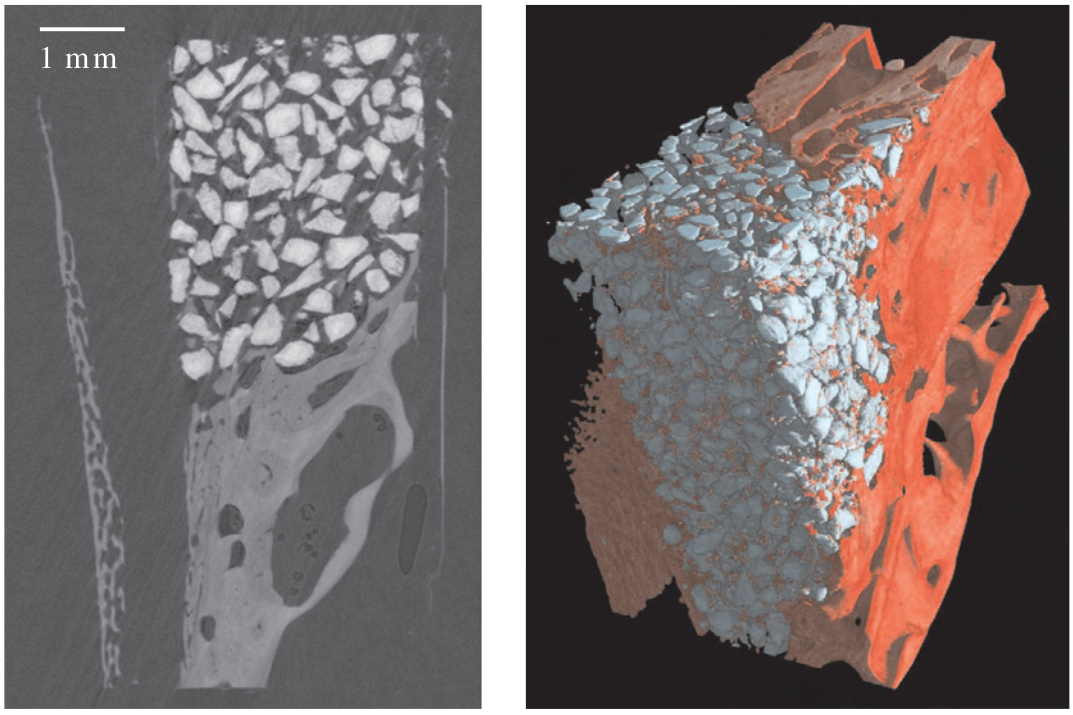

FIG. 10: Left – tomographic slice of a sheep jawbone with ceramic particles (light grey, bone in grey, the remaining area is the resin with some porosity) three months after implantation, right: volume rendering of the segmented data set, showing ceramic particles (white) and detected bone (grey). Newly formed bone can be identified between the particles [69].

print: BW, web: color

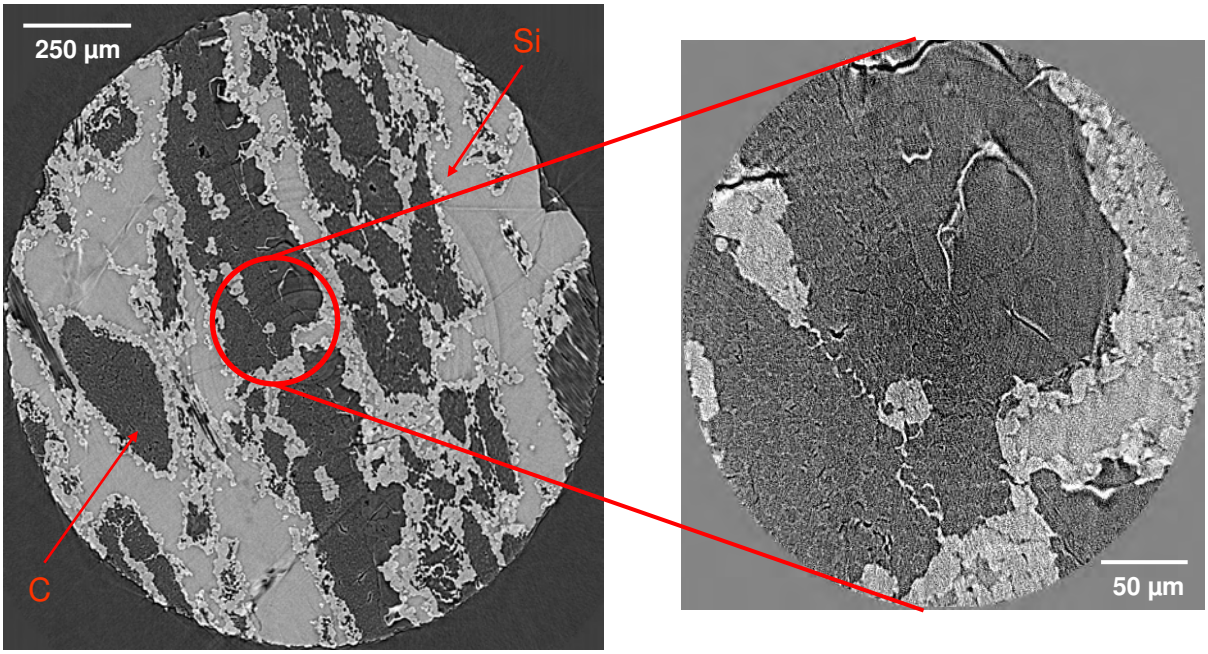

FIG. 11: Cross sections of a fibre reinforced C/SiC ceramic (Fraunhofer ISC, Dr. J. Meinhardt), the left image is taken with a resolution of < 4 μm (10% of the MTF, effective pixel size of 1.5 μm, 17 keV X-ray energy, CWO scintillating single crystal), the right image (local tomography) uses a resolution of < 2 μm (determined via a Siemensstar, 0.6 μm effective pixel size, LuAG:Eu scintillating single crystal 4 μm thick): carbon fibres, silicon, micro-cracks and SiC crystals are visible [43].

print: BW, web: color

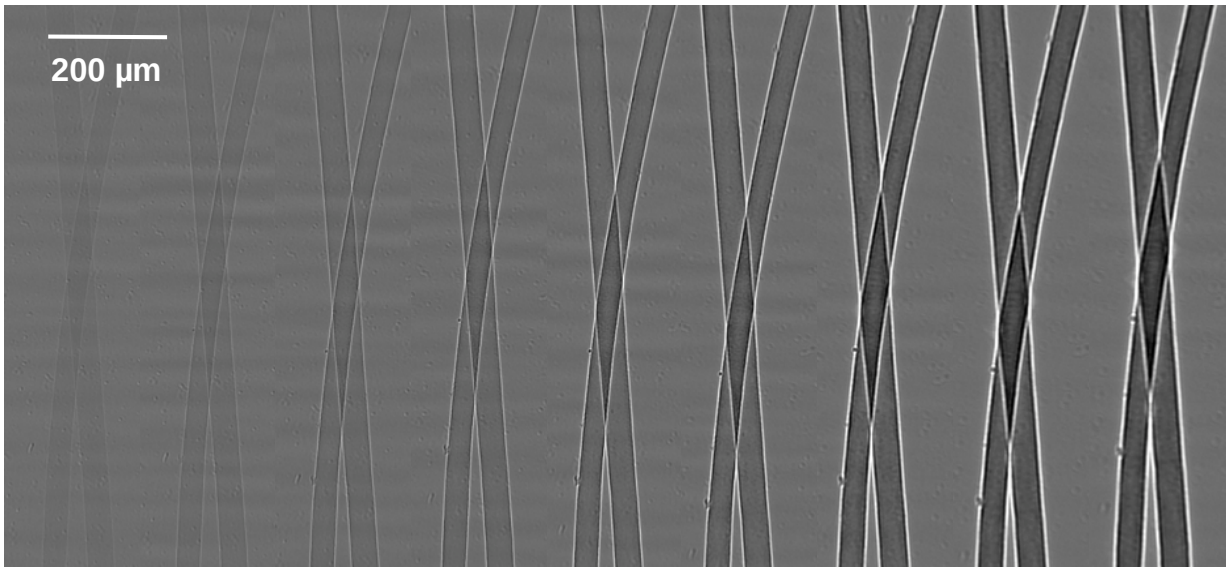

FIG. 12: Images of two hairs taken at different sample-to-detector distances ranging from 20 mm to 1140 mm (E = 20 keV photon energy, LuAG:Eu scintillator 4 μm thick, effective pixel size of 0.6 μm, < 2 μm resolution determined via a Siemensstar).

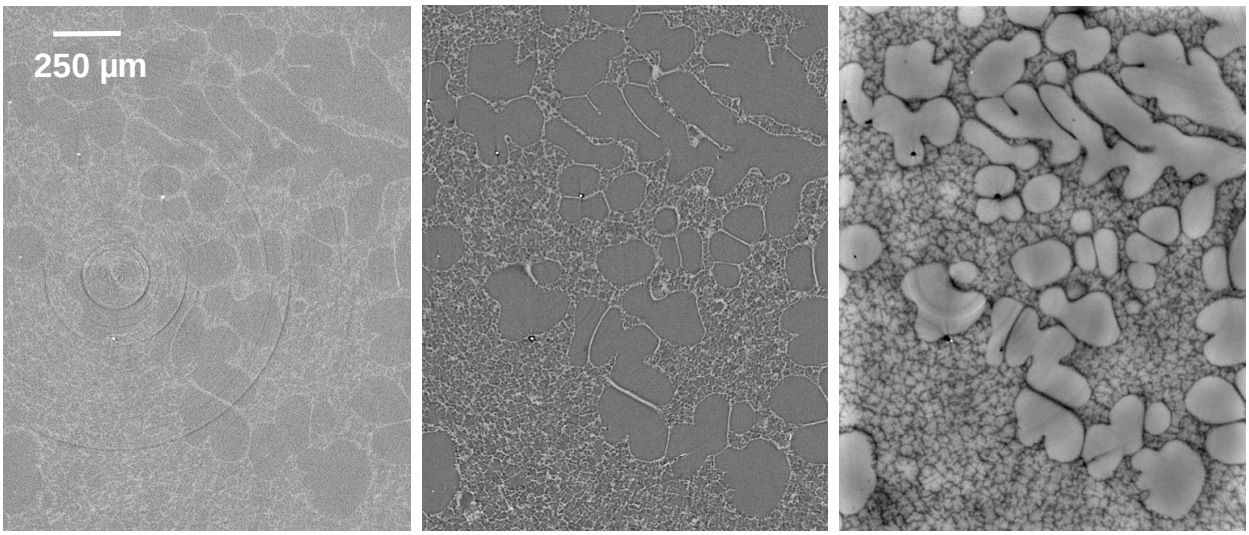

FIG. 13: Left: absorption tomogram from a specimen consisting of the alloy AZ91 (magnesium and aluminium, similar attenuation coefficients) recorded at D = 15 mm, middle: same slice but as phase contrast tomography calculated from Fresnel-propagated projection images recorded at D = 433 mm (edge enhancement), right: holotomography of this slice combining the propagation distances D = 15 mm, 144 mm, 433 mm and 720 mm (E = 23 keV, effective pixel size 1.6 μm, < 4 μm resolution – 10% of the MTF, CWO screen) [81].

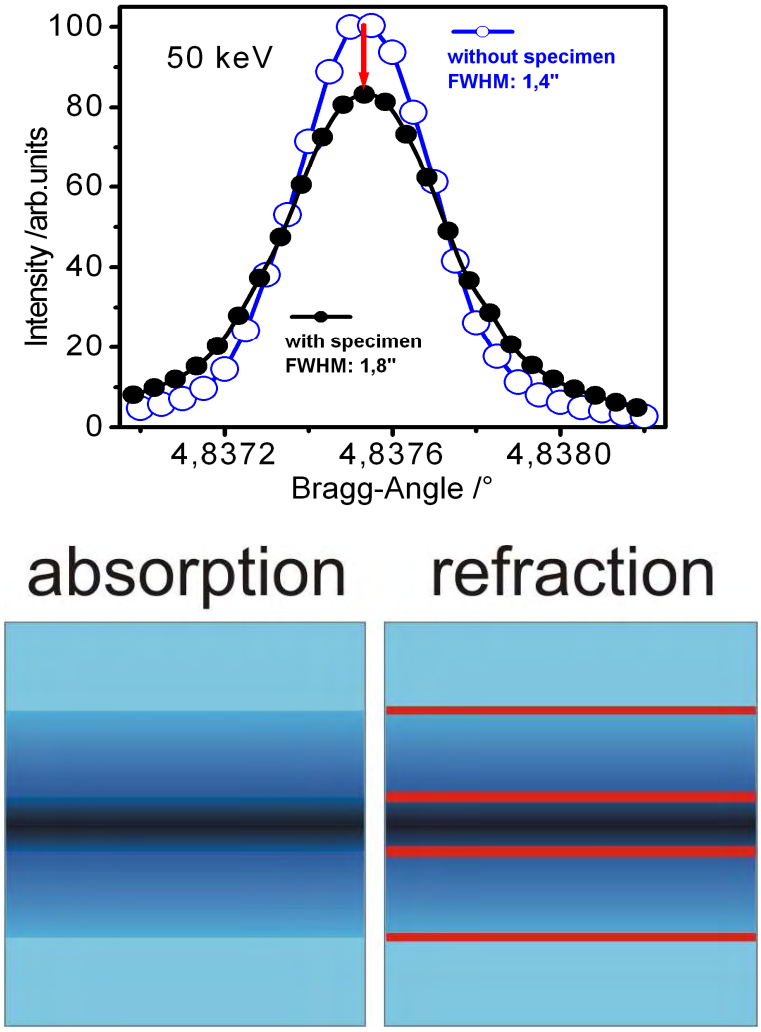

FIG. 14: Top: the Rocking Curves of the Si(111) single crystal pair in symmetric configuration at 50 keV with specimen (filled dots) and without specimen (open circles) between the two crystals. The area under the curves is set to equal. Bottom: demonstration of the refraction enhanced contrast (cf. figure 5).

print: BW, web: color

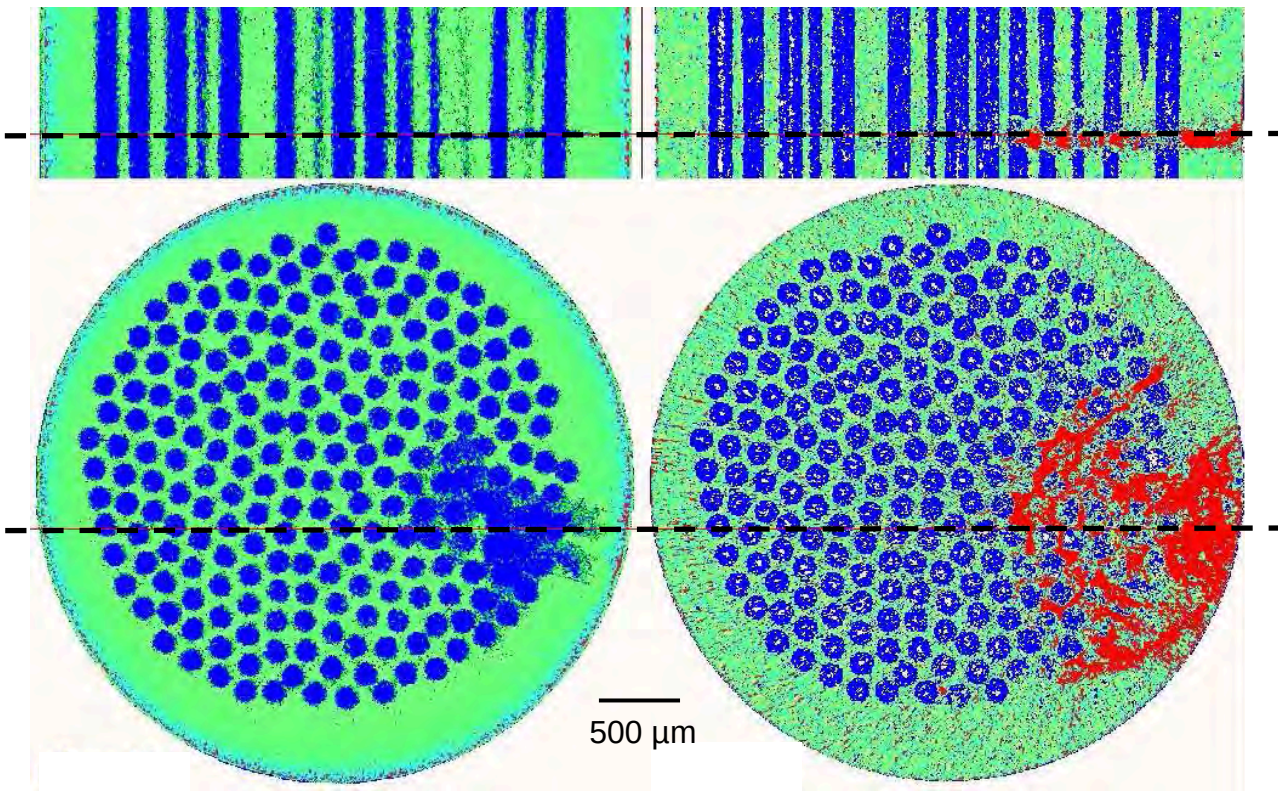

FIG. 15: Tomographic reconstructions of a SiC reinforced titanium fibre structure (3.5 mm diameter), SiC-fibres are visible as black (blue) discs, the titanium matrix is the main area (green). Left: Reconstruction of the absorption measurement (laboratory CT, 100 kV, 4.7 μm effective pixel size), sagittal plane (top) of the specimen as indicated by the dashed line in the bottom (axial plane) – a crack can be distinguished in the right part of the sample. Right: reconstruction of the corresponding slice with refraction enhanced contrast (BAM*line*, 50 keV, 5.3 μm effective pixel size). The crack distribution in the matrix (red area) is much more larger than it appears in the absorption image [58].

print: BW, web: color

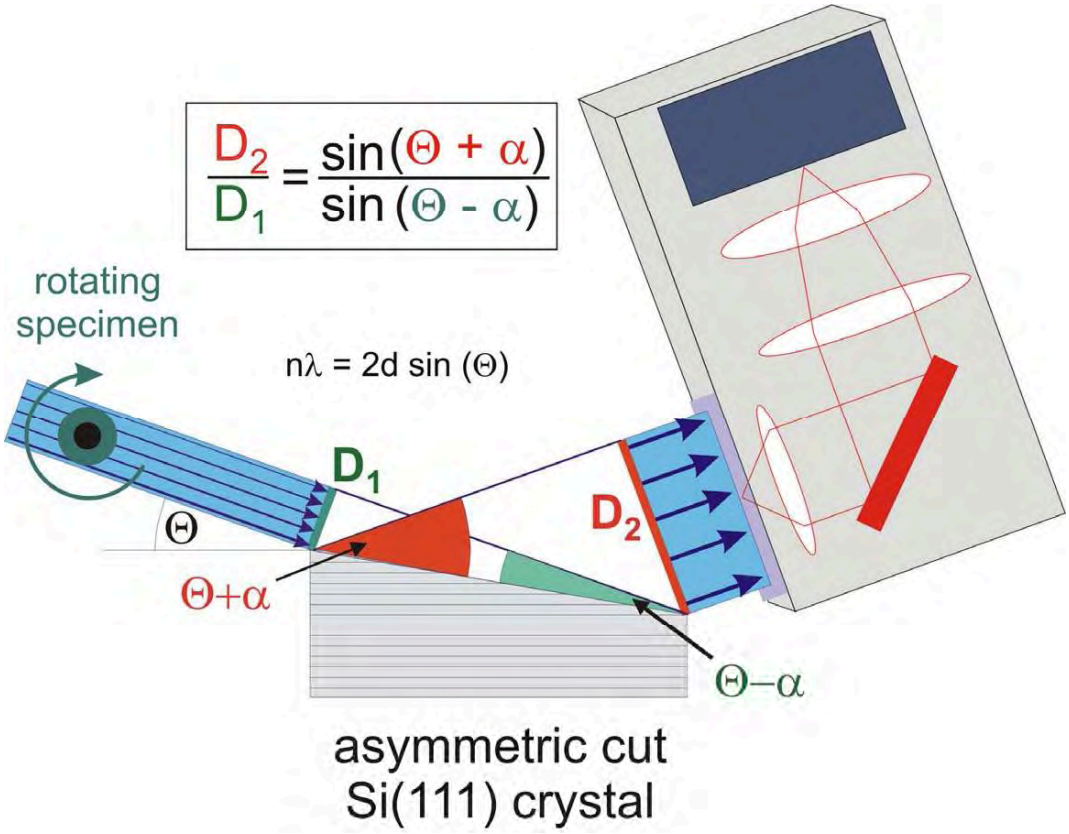

FIG. 16: Principle of one-dimensional beam width magnification by use of an asymmetric cut Bragg crystal. D_1 and D_2, width of the incoming and reflected beam, respectively; λ: X-ray wavelength, d: distance between net planes of the crystal, Θ: gracing angle between beam and net plans, α: angle between surface and net planes of the crystal.

print: BW, web: color

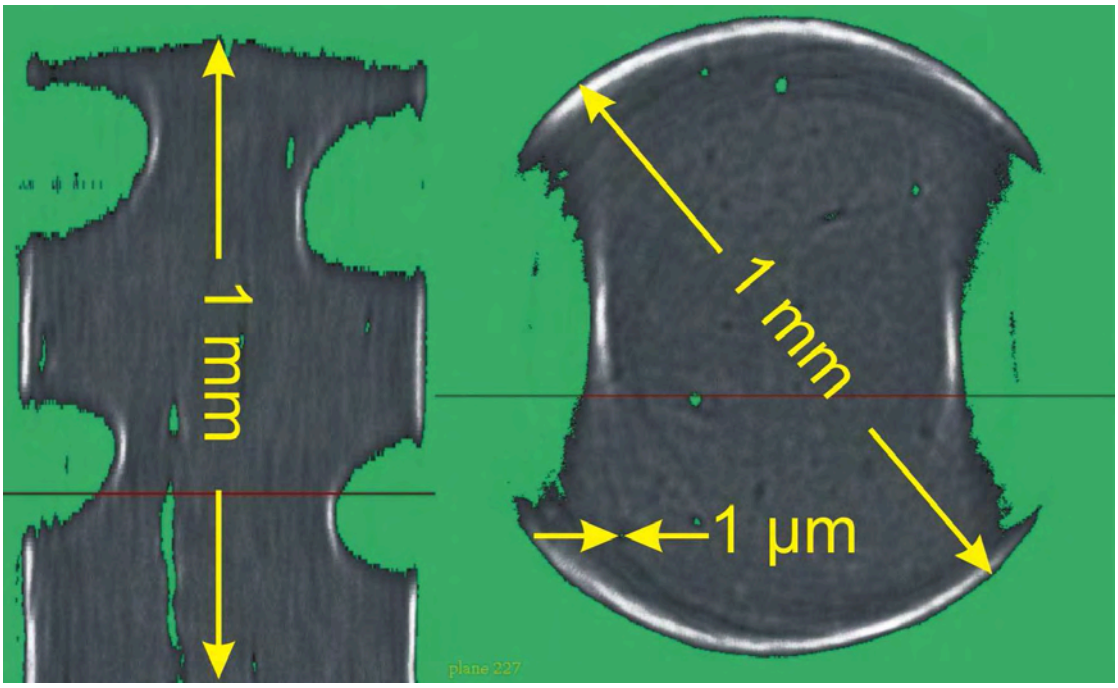

FIG. 17: Nano Refraction CT using magnification by asymmetric Bragg reflection: reconstructed sagittal (left) and axial (right) cross section of a steel micro drill from projection images taken with 19 keV X-ray energy. The refraction contrast at the outer edges and around the pores can be seen. One tubular pore below 1 μm in diameter is indicated by the two arrows on the lower right. The gray level profile along the connecting line of the arrows is given in fig. 18.

print: BW, web: color

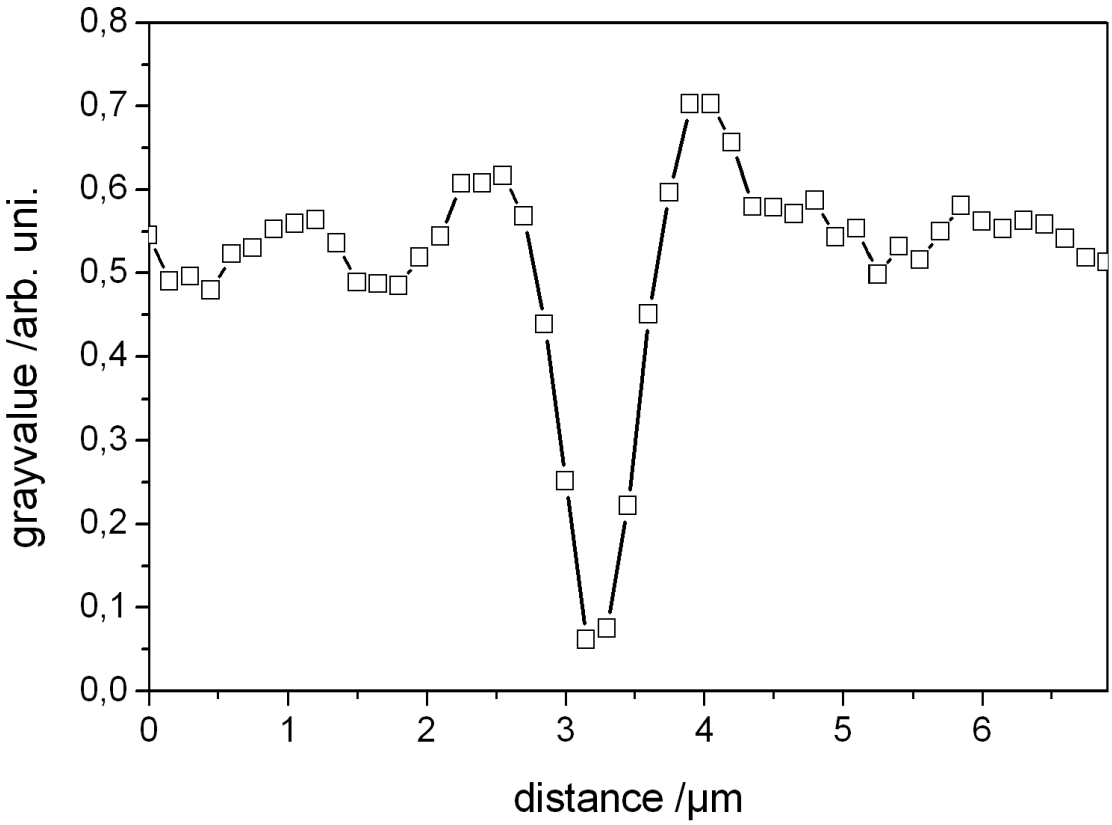

FIG. 18: The gray level profile along the line indicated by the two arrows on the lower right of fig. 17 demonstrates the true submicrometer resolution achieved by using asymmetric Bragg reflections. The pore between the heads of the two arrows in fig. 17 is around 1 μm in size and can clearly be identified in the gray level profile.

APPENDIX B: TABLES

Optics	Resolution FieldOfView
Olympus *Plapon* 1.25x (NA = 0.04, 2.5x)	R > 10.8 μm (5.4 μm) 11.1 mm x 11.1 mm
Olympus *Plapon* 2x (NA = 0.08, 4x)	R > 6.8 μm (3.4 μm) 6.9 mm x 6.9 mm
Olympus *Uplsapo* 4x (NA = 0.16, 8x)	R > 3.4 μm (1.7 μm) 3.4 mm x 3.4 mm
Olympus *Uplsapo* 10x (NA = 0.40, 20x)	R > 1.4 μm (0.7 μm) 1.4 mm x 1.4 mm
Olympus *Uplsapo* 20x (NA = 0.75, 40x)	R > 0.6 μm (0.3 μm) 0.6 mm x 0.6 mm

TABLE I: The microscope detector's approx. values for the field of view and max. resolution R (with effective pixel size in brackets) when combining different Olympus objectives (numerical aperture and effective magnification factor given in brackets) with a 2x eye-piece and the Princeton Instruments CCD camera *VersArray: 2048B* (2048x2048, 13.5 μm).

CRYSTAL	WAVELENGTH (MAX. EMISSION) [nm]	DENSITY [g/cm^3]	LIGHT YIELD [Ph/MeV]	RISE TIME [ps]	AFTER GLOW
CWO	$\sim$ 495	7.9	19840	$<$ 30	0.014 [% after 20 ms]
BGO	$\sim$ 480	7.1	$\sim$ 9000	$\sim$ 30	0.005 [% after 6 ms]
LuAG:Eu	580, 700	6.7	11000	$<$ 1000	1.0 [% after 32 ms]
LSO:Ce	404	7.4	30000	$\sim$ 30	–

TABLE II: Characteristics of the scintillating materials used at BAM*line*, origins of individual values are given in [43], for the attenuation coefficients see fig. 7.

Camera Optics	*VersArray: 1300B* (1340x1300, 20 μm)	*VersArray: 2048B* (2048x2048, 13.5 μm)
Rodenstock *TV-Heligon* f = 21 mm, NA = 0.5, 8.6x	3.1 mm x 3.0 mm R > 4.6 μm (2.3 μm)	3.2 mm x 3.2 mm R > 3.2 μm (1.6 μm)
Rodenstock *TV-Heliflex* f = 50 mm, NA = 0.45, 3.6x	7.4 mm x 7.2 mm R > 11.2 μm (5.6 μm)	7.7 mm x 7.7 mm R > 7.6 μm (3.8 μm)
Rodenstock *XR-Heliflex* f = 100 mm, NA = 0.33, 1.8x	14.9 mm x 14.4 mm R > 22.2 μm (11.1 μm)	15.4 mm x 15.4 mm R > 15.0 μm (7.5 μm)

TABLE III: The macroscope detector's approx. values for the field of view and max. resolution R (with effective pixel size in brackets) when combining different Rodenstock optics (focal length, numerical aperture, effective magnification factor are given in brackets [54]) with the Nikon *Nikkor 180/2.8 ED* (f = 180 mm) objective and corresponding Princeton Instruments CCD camera.